ChemistryEurope

ChemistryEurope
Excellence in Chemistry Research Worldwide

REVIEW OPEN ACCESS

Strategies for Redox Potential Regulation of Organic Molecules in Nonaqueous Redox Flow Batteries

Li Wang[1] | Yuanlin Zou[2] | Qinwen Zhu[1] | Yu Qin[1] | Jiayi Huang[1] | Zhong Jin[2] | Yichao Yan[1] | Jia Zhu[1]

[1]School of Sustainable Energy and Resources, Jiangsu Key Laboratory of Artificial Functional Materials, Frontiers Science Center for Critical Earth Material Cycling, Nanjing University, Nanjing, Jiangsu Province, P. R. China | [2]School of Chemistry and Chemical Engineering, State Key Laboratory of Coordination Chemistry, MOE Key Laboratory of Mesoscopic Chemistry, MOE Key Laboratory of High Performance Polymer Materials and Technology, Jiangsu Key Laboratory of Clean Energy Catalysis and Intelligent Green Chemical Engineering, Suzhou Key Laboratory of Green Intelligent Manufacturing of New Energy Materials and Devices, Tianchang New Materials and Energy Technologies Research Center, Institute of Green Chemistry and Engineering, Nanjing University, Nanjing, Jiangsu Province, P. R. China

Correspondence: Zhong Jin (zhongjin@nju.edu.cn) | Yichao Yan (ychyan@nju.edu.cn)

Received: 19 December 2025 | **Revised:** 6 March 2026 | **Accepted:** 9 March 2026

Keywords: high voltage | NAORFBs | organic active molecules | potential regulation | structure–activity relationship

ABSTRACT

Redox flow batteries (RFBs) are a promising solution for large-scale and sustainable energy storage. However, aqueous RFBs (ARFBs) are limited by the narrow electrochemical window of water (1.23 V), making it difficult to achieve high voltage output. Nonaqueous organic RFBs (NAORFBs), leveraging the wide electrochemical stability window of nonaqueous solvents (3–5 V) and the structural tunability of redox-active organic molecules (ROMs), possess the potential to construct high voltage and energy density RFBs. Nevertheless, issues including poor redox potential matching of ROMs and the imbalance between potential and stability seriously restrict the improvement of the actual operating voltage and energy density of the batteries. Therefore, the targeted regulation of redox potentials has become a critical breakthrough for the development of NAORFBs. This review focuses on the potential tuning mechanisms of organic molecules, with an emphasis on strategies for elevating the redox potential of cathode materials and lowering those of anode materials. We summarize recent advances in the structural modification of ROMs and analyze how these strategies influence the redox potential and stability. By centering on molecular design principles for redox potential control, this work offers mechanistic insights and future directions for the development of high-voltage NAORFBs.

1 | Introduction

In the process of the global transition toward a cleaner and low-carbon energy structure, renewable energy sources such as wind, solar, and tidal power have experienced leapfrog growth in installed capacity [1–3]. According to statistics from the International Renewable Energy Agency (IRENA), the global installed capacity for renewable energy power generation reached 4448 GW in 2024, accounting for over 46% of the total global installed capacity. This proportion is projected to exceed 55% by 2030 [4–8]. However, the inherent intermittency and instability of renewable energy sources often lead to issues such as grid frequency fluctuations and voltage deviations after their integration into the power grid [9]. This underscores the urgent demand for large-scale and long-duration energy storage technologies [10, 11]. Therefore, developing energy storage systems (ESSs) to store surplus energy when abundant and utilize it to enhance grid stability when scarce is of paramount importance [12].

Current mainstream energy storage technologies are incompatible with large-scale renewable energy applications. Lithium-ion batteries rely on scarce lithium/cobalt, with issues like cost volatility, short cycle life (<3000 cycles), and incompatibility with 10,000-h long-duration storage [13–22]. On the other hand, pumped hydro storage is limited by geography and long construction cycles (5–10 years), making flexible deployment hard [23–27].

Among various large-scale energy storage technologies, redox flow batteries (RFBs) have emerged as a prominent research focus due to their unique advantages such as the decoupling of capacity and power, long cycle life, and strong environmental adaptability [28, 29]. The concept of flow batteries was first introduced by Thaller at the Jet Propulsion Laboratory (JPL) in 1974, aiming to achieve reversible conversion between electrical and chemical energy through the circulation of liquid active materials [30–32]. Figure 1 demonstrates the schematic diagram of RFB. The core components of RFBs include the electrochemical stack, which consists of high-surface-area porous carbon electrodes, ion exchange membranes, and conductive bipolar plates, along with an electrolyte storage and circulation system that includes electrolyte storage tanks, peristaltic pumps, and temperature control modules [33]. The flow battery system utilizes two redox modes (p-type/n-type) and two electrode roles (catholyte/anolyte) in the electrochemical cell. p-type materials undergo oxidation (electron loss) during charge/discharge, while n-type materials undergo reduction (electron gain). Catholyte refers to the electrolyte in contact with the cathode (positive electrolyte), and anolyte refers to the electrolyte in contact with the anode (negative electrolyte).

The working principle involves pumping electrolytes with dissolved redox-active materials through electrodes [34]. These active materials undergo reversible oxidation–reduction reactions on the electrode surfaces, while the ion exchange membranes prevent the mixing of electrolytes and maintain charge balance [35]. This makes RFBs a key technology for mitigating the intermittency of renewable energy integration and enhancing grid stability and energy absorption capacity [36].

Technologically, flow batteries have evolved iteratively, advancing from aqueous systems to nonaqueous inorganic systems and then to nonaqueous organic systems [37]. Early aqueous flow batteries, such as vanadium, iron–chromium, and zinc–bromine systems, achieved significant research and application advancements, offering high safety and long cycle life (>10,000 cycles). However, they were limited by the decomposition voltage of water (≈1.23 V), resulting in energy densities generally below 40 Wh L^{-1} [38]. To overcome the potential window limitation of aqueous solvents, researchers turned to nonaqueous inorganic flow batteries. In 1988, Matsuda et al. employed $Ru(bpy)_3^{2+/3+}$ as the active material for both the positive and negative electrodes, marking the first report of a NARFB. Thanks to the well-suited high and low redox potentials of $Ru(bpy)_3^{2+/3+}$, the battery achieved an open-circuit voltage (OCV) of 2.6 V over twice that of ARFBs [39]. Subsequently, researchers have also developed a series of NARFBs based on metal complexes, including $Ru(acac)_3$, $V(acac)_3$, $Cr(acac)_3$, $Fe(bpy)_3^{2+/3+}$, $Ni(bpy)_3^{2+/3+}$, and $UO_2(acac)_2$, significantly improving energy density [40–44]. Precious metal-based complexes, such as those based on ruthenium and rhodium, are extremely costly, with prices reaching hundreds of US dollars per gram [45]. Moreover, these complexes are highly toxic and exhibit bioaccumulative properties. As a result, these systems have remained at the experimental stage and have not achieved industrial breakthrough [46]. It is precisely the limitations of traditional systems that have driven the rise of NAORFBs. These batteries leverage the synergistic advantages of organic active materials and nonaqueous solvents, becoming a key solution to the above challenges [47]. Organic molecules have abundant raw materials and can be derived from petrochemical by-products or biomass resources. They are not only low-cost and biodegradable but also possess excellent molecular structural designability. This has increased the energy density of NAORFBs to 80–120 Wh L^{-1}, which is two to three times that of ARFBs [48].

From the perspective of core performance requirements, high voltage is the key to overcoming the energy density bottleneck of NAORFBs. According to the battery energy density calculation formula

$$\text{Energy density (Wh L}^{-1}) = \frac{nCVF}{\mu_v} \quad (1)$$

where n is the number of electrons stored in the redox-active materials, C is the concentration of redox-active materials in the electrolyte solution (mol L^{-1}), F is the Faraday constant (96,485 C mol^{-1}), V is the cell voltage (V) indicating the difference in the redox potential of the cathode and anode, and μ_v is the volume factor. Energy density is directly related to the OCV; notably, the OCV of NAORFBs adheres to the core relationship: $OCV = E_+ - E_-$, where E_+ denotes the redox potential of the organic molecule in the cathode and E_- represents the redox potential of the organic molecule in the anode. Thus,

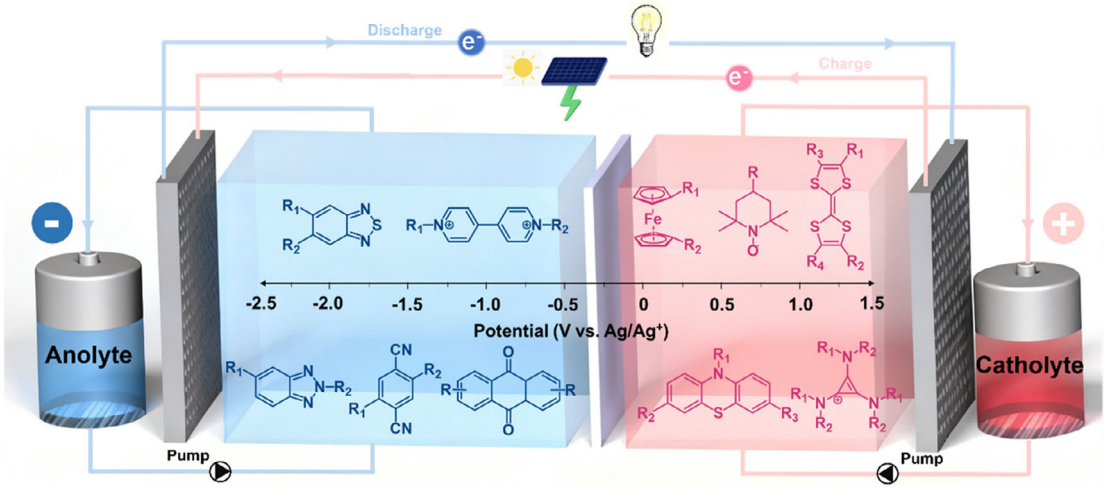

FIGURE 1 | Schematic diagram of NAORFBs and potentials of selected redox compounds as demonstrated in NAORFBs.

the essence of achieving a high cell voltage for NAORFBs lies in the rational pairing of organic molecules [49]. Although NAORFBs have made initial progress in high voltage and long cycling in recent years, there are still some bottlenecks in current research on the potential regulation of organic molecules. For instance, the mechanisms are fragmented, the quantitative relationship between the structure of organic molecules and their potential has not yet developed a systematic theory, and the regulatory rules remain unclear. Consequently, regulating the redox potential of organic molecules emerges as the core prerequisite for constructing high-voltage NAORFBs.

This review centers on the potential regulation mechanisms of organic molecules as its main thread, focusing on the goal of developing high-voltage NAORFBs for a systematic analysis. We divide this review into three sections; the first section provides a detailed description of the fundamental theories of organic molecule potential regulation, establishing a theoretical framework for potential control. The second and third sections, combined with experimental data, respectively, introduce the potential regulation mechanisms of certain high-potential organic cathodes and low-potential organic anodes. Finally, the review summarizes current challenges and prospects for future directions, providing theoretical guidance and technical insights for advancing high-voltage NAORFBs from fundamental research toward large-scale application. Figure 1 shows the schematic diagram of NAORFBs and potentials of selected redox compounds as demonstrated in NAORFBs.

2 | Fundamental Theories of Organic Molecule Potential Regulation

2.1 | Core Definition and Reference of Organic Molecule Redox Potentials in Nonaqueous Systems

2.1.1 | The Essence of Redox Potential

Redox potential is fundamentally an energy related to the gain or loss of electrons by a molecule under given conditions, that is, the thermodynamic tendency during the oxidation or reduction reaction of the molecule. The value of this potential is determined by the Gibbs free energy difference between the molecule's oxidized (Ox) and reduced (Red) states, which can be calculated as follows:

$$\Delta G = -nFE \tag{2}$$

where ΔG is the Gibbs free energy difference before and after the redox reaction, n is the number of electrons transferred, F is the Faraday constant, and E represents the corresponding oxidation or reduction potential.

The above calculation represents the thermodynamic potential under ideal conditions. However, in practical applications, the determination of redox potential requires specific conditions, including solvent, supporting electrolyte, selected reference electrode, and electron transfer resistance. These factors may cause experimental values of redox potentials to deviate from the theoretical thermodynamic values [50].

To more accurately describe the redox potential under practical conditions, we introduce the concept of the standard electrode potential (E^{θ}). E^{θ} refers to the electrode potential measured under standard conditions (25°C, concentrations of reactants and products at 1 M, and gas pressure at 1 atm). It represents the thermodynamic tendency of a redox couple under ideal conditions and is commonly used to compare the relative strengths of different redox pairs [51]. Under nonstandard conditions, the redox potential adjusts with changes in activity, temperature, and solvent polarity, which can be quantified using the Nernst equation:

$$E = E^{\theta} - (RT/nF)\ln a_R^{v_R}/a_O^{v_o} \tag{3}$$

where R is the gas constant (8.314 J/mol·K), T is the absolute temperature (K), a is the activity of reactants and products, and v is stoichiometric coefficient.

In conclusion, the thermodynamic nature of redox potential is quantified through Gibbs free energy and the Nernst equation. These theoretical tools lay the foundation for the potential regulation of high-voltage organic molecules in NAORFBs.

2.1.2 | Potential Reference in Nonaqueous Systems

Since the absolute value of a single electrode potential holds no inherent meaning, it is the potential difference between electrodes that has clear physical significance. Therefore, selecting a stable reference electrode is essential. Ideally, a reference electrode should possess excellent chemical and electrochemical stability, exhibit minimal polarization, or be nonpolarizable, ensuring that its potential remains unaffected by small current fluctuations. It should also provide a stable, nondrifting potential and demonstrate good redox reversibility, with excellent potential reproducibility [52].

In practice, it is challenging to satisfy all of these requirements simultaneously, and thus, a suitable reference electrode must be selected according to different application scenarios. For example, in aqueous battery systems, commonly used reference electrodes include the standard hydrogen electrode (SHE) and metal salt electrodes such as silver/silver chloride (Ag/AgCl) and saturated calomel electrode (SCE). However, nonaqueous electrolytes are typically based on organic solvents such as propylene carbonate or ethers that lack hydrated hydrogen ions (H_3O^+), making it impossible to use SHE or other water-based reference electrodes (e.g., Ag/AgCl or SCE). These aqueous reference electrodes present issues such as high liquid junction potentials, electrolyte contamination, and blockages in molten states [53]. Metal-ion electrodes such as Li/Li^+ avoid these problems because they are based directly on the ion chemistry of the nonaqueous system. Moreover, the Li/Li^+ electrode has better compatibility with nonaqueous electrolytes, especially those containing lithium salts (e.g., $LiPF_6$ or LiTFSI). The potential of the reference electrode is defined based on the reversible reaction ($Li^+ + e^- \rightleftharpoons Li$). Since both the reference electrode and the electrolyte share the common component (Li^+), a thermodynamic equilibrium can be established, leading to a well-defined potential for the reference electrode. Therefore, the Li/Li^+ reference electrode is highly compatible with nonaqueous systems, ensuring the stability of the electrolyte [54].

In practical applications, the silver/silver ion reference electrode (Ag/Ag^+) is also commonly used, particularly in organic solvent systems without lithium salts. On the other hand, the ferrocene electrode (Fc/Fc^+) maintains a stable potential that does not

change with variations in solvent or supporting electrolyte, making it highly stable [55]. However, it is not used as a reference electrode but as an internal reference, directly added to the electrolyte. When the potential of the measured electrolyte does not overlap with that of ferrocene, excellent results can be achieved.

2.2 | Core Principles of Structure-Regulated Potential in Organic Molecules

The potential of organic molecules is closely related to the gain or loss of electrons. Therefore, the redox potential is inherently connected to the molecular electronic structure, including the electron affinity, ionization energy, and frontier orbital energy levels. These characteristics depend on the composition and structure of the molecule. This section will focus on the three key effects of molecular structure on potential regulation.

2.2.1 | Inductive Effects

The inductive effect, based on electronegativity differences between atoms or groups, transmits electron cloud displacement through σ bonds, directly influencing the electron distribution of organic molecules and thereby regulating their redox potentials. From the perspective of molecular orbital theory, the oxidation potential is negatively correlated with the energy of the highest occupied molecular orbital (HOMO); the higher the HOMO energy, the easier it is for the molecule to lose electrons, and the lower the oxidation potential. In contrast, the reduction potential is negatively correlated with the energy of the lowest unoccupied molecular orbital (LUMO); the lower the LUMO energy, the easier it is for the molecule to accept electrons, and the higher the reduction potential [56].

Electron-donating groups (EDGs) repel the electron cloud through the electron-donating inductive effect (+I effect), increasing the electron cloud density of the molecule and raising the energies of HOMO and LUMO, resulting in a decrease in its redox potential. In contrast, electron-withdrawing groups (EWGs) pull the electron cloud of σ bonds through the electron-withdrawing inductive effect (−I effect), reducing the overall electron cloud density of the molecule. This lowers the HOMO energy and decreases the LUMO energy, ultimately leading to an increase in the redox potential. Taking methyl-substituted (H_3C-) and fluoro-substituted (-F) benzothiadiazole as examples (Figure 2a), the methyl group exerts a +I effect, pushing electron density toward the core and lowering its redox potential, while the fluoro group exerts a −I effect, pulling electron density away, thus lowering its redox potential [57].

2.2.2 | Conjugation Effects

The continuous overlap of π bonds in molecules forms a delocalized electron system. The conjugation effect directly affects the ease of electron gain or loss in molecules by altering the range and distribution of electron delocalization within the molecule, thereby regulating its redox potential [58]. Its regulatory effect on potential is often more significant than that of the inductive effect, and it is closely related to the conjugation length and the conjugation electronic effects (+C or −C) of EDGs/EWGs [59, 60].

In a conjugated system, electron delocalization narrows the energy gap between the HOMO and the LUMO, while the conjugation effects of EDGs/EWGs can further modify the orbital energies. Specifically, EWGs withdraw electrons from the conjugated system through the electron-withdrawing conjugation effect (−C effect), thereby increasing the redox potential. In contrast, EDGs inject electrons into the conjugated system via the electron-donating conjugation effect (+C effect), which helps elevate the energy of their HOMO. Taking cyano (–CN)- and methoxy ($–OCH_3$)-substituted azobenzene as examples (Figure 2a), the cyano group possesses strong electron-withdrawing properties and withdraws electron density from the conjugated system through the −C effect, thus significantly increasing its redox

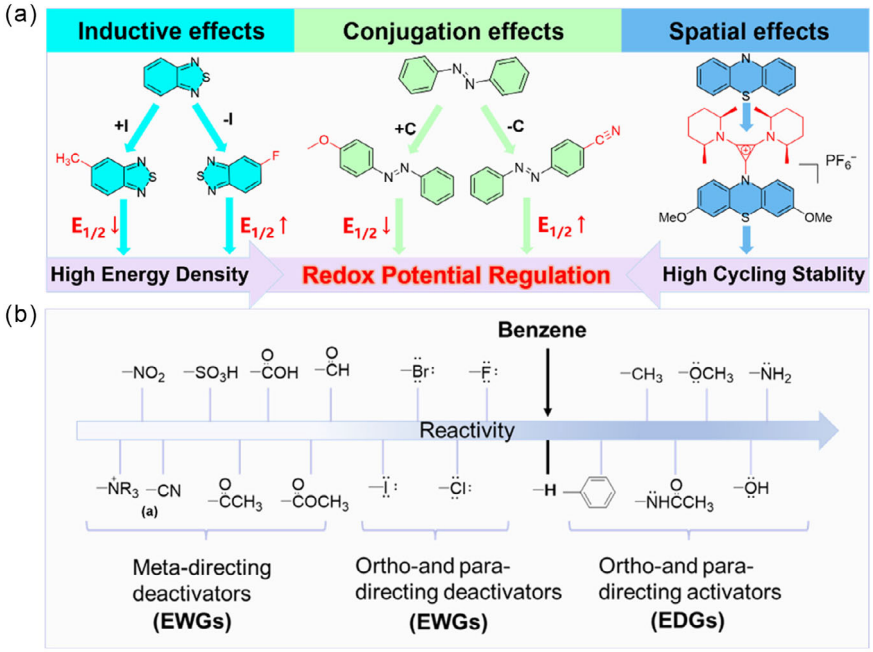

FIGURE 2 | (a) Inductive effect, conjugation effect, and spatial effect schematic diagram. (b) Classification of substituent effects.

potential [61, 62]. Meanwhile, the methoxy group exhibits strong electron-donating characteristics and enhances the electron cloud density of the conjugated system via the +C effect, leading to a decrease in its redox potential. Notably, the longer the conjugated chain, the more sufficient the electron delocalization, and the more pronounced the conjugation effect. Additionally, the planarity of the conjugated system is a prerequisite for effective electron delocalization: The better the planarity, the stronger the conjugation effect, and the more regular the regulation of the molecular redox potential [63].

In practical applications, the conjugation effect often acts synergistically with the inductive effect, and the comparison of their strengths determines the final direction of the molecular electronic effect. The strength of the actual electronic effects of some common substituents is shown in Figure 2b [64].

2.2.3 | Spatial Effects

Steric hindrance does not directly participate in electron transfer; instead, it indirectly affects electron delocalization and orbital energies by altering the molecular configuration (especially the planarity of conjugated systems), thereby regulating the potential. When bulky groups (such as polysubstituted aryl groups, tert-butyl groups, etc.) are present in the molecule, the repulsive interactions between these groups disrupt the coplanarity of the conjugated system [65]. Taking cyclopropenyl cation-substituted phenothiazine derivatives as an example (Figure 2a), the 2,6-dimethylpiperidine (DMPP) group plays a crucial role in regulating molecular geometric conformation, maintaining oxidation state stability, and improving long-cycle performance. In terms of geometric conformation, the moderate steric hindrance of the DMPP group can prevent excessive torsion between the cyclopropene ring and the phenothiazine ring caused by overly large substituents. This incomplete torsion not only retains sufficient conjugation to ensure a high first oxidation potential but also avoids the uneven electron cloud distribution that may be induced by excessive conjugation, laying a structural foundation for the reversibility of the two-electron cycle. Meanwhile, the steric hindrance effect can also inhibit close-range intermolecular interactions (such as aggregation or polymerization) of oxidized molecules, preventing decreased solubility caused by molecular aggregation [66, 67].

2.3 | External Regulation of Organic Molecule Potentials by Nonaqueous Electrolytes

The potential of organic molecules is not solely determined by their inherent structure; the supporting electrolyte can modify the electronic state of the molecule through ion coordination effects, which in turn influences the electrochemical potential. The supporting electrolyte plays a significant role in altering the redox potential, electrochemical stability, and overall performance of the electroactive material. Zhang et al. investigated the solvation behavior of 2,1,3-benzothiadiazole (BzNSN) as a typical model system across various supporting electrolytes [68]. As illustrated in Figure 3a, by systematically varying the composition of the supporting salt, particularly the size of the cation, the redox potential of BzNSN exhibited a noticeable negative shift, from −1.63 to −1.82 V vs. Ag/Ag^+. This highlights the critical role of cation size in modulating the potential. Specifically, smaller cations (Li^+) are more tightly coordinated with the charged BzNSN molecule, leading to stronger interactions that increase the redox potential while simultaneously reducing stability. Moreover, this effect intensifies with higher concentrations of supporting salts. In contrast, larger cations (NEt_4^+) interact weakly and are situated further from the active material, thereby enhancing stability, improving electrochemical performance, and further decreasing the redox potential. To gain in-depth insight into the regulatory mechanism of supporting salt cations on the electrochemical behavior of redoxmers, the research team further verified the interaction law between cations and redox-active species through concentration gradient experiments. Using cyclic voltammetry, they investigated the electrochemical response of BzNSN in two types of supporting electrolytes, namely, 0.1–1.0 M LiTFSI (Figure 3b) and NEt_4TFSI (Figure 3c). The results showed that the type of cation significantly affected the sensitivity of BzNSN's redox potential to concentration. In the LiTFSI system, as the salt concentration increased from 0.1 to 1.0 M, the redox potential of BzNSN gradually increased, shifting upward from −1.72 to −1.61 V with a total shift of 110 mV. In contrast, in the NEt_4TFSI system, although the redox potential of BzNSN itself was significantly lower (with an initial potential of −1.84 V vs. Ag/Ag^+), the magnitude of its change with concentration was greatly reduced when the supporting salt concentration also increased from 0.1 to 1.0 M; the potential only showed a slight positive shift of 40 mV. This significant difference in the concentration effect indicates that the interaction strength between Li^+ and BzNSN molecules is much higher than that between NEt_4^+ and BzNSN, further confirming the view that the type and concentration of supporting salts are the core factors regulating the electrochemical performance of redox-active species.

2.4 | Data Normalization

Unification of reference standards is the core to ensure the comparability of potential data across different studies. As mentioned earlier, the absolute value of a single electrode potential is meaningless. To ensure comparability between different studies, a stable electrode must be selected as the reference electrode, and all potential data must clearly specify the reference electrode (e.g., 3.6 V vs. Li/Li^+) to avoid ambiguity. If different literatures use different reference standards (e.g., Ag/Ag^+ and Fc/Fc^+), the data can be converted between them using standard conversion formulas. This unification facilitates cross-laboratory comparison of the potentials of organic molecules, avoids deviations caused by differences in reference electrodes, and thus enables accurate analysis of regulatory mechanisms [69]. The specification of electrolyte conditions is a key step in data normalization. It is essential to clearly state the solvent type (e.g., PC/DMC = 1:1), supporting electrolyte concentration (e.g., 1 M LiTFSI), and test temperature (e.g., 25°C), as these factors directly affect potential measurement. By specifying these conditions, potential deviations caused by differences in electrolytes can be avoided, the comparability of different studies is ensured, and guidance is provided for the practical assembly of batteries [70]. Table 1 shows the common reference electrode potential conversion.

Through density functional theory (DFT) calculations, the following parameters of organic molecules can be studied: structure optimization, solvation free energy, electrostatic potential, molecular orbitals, redox potential, UV–Vis spectrum simulation,

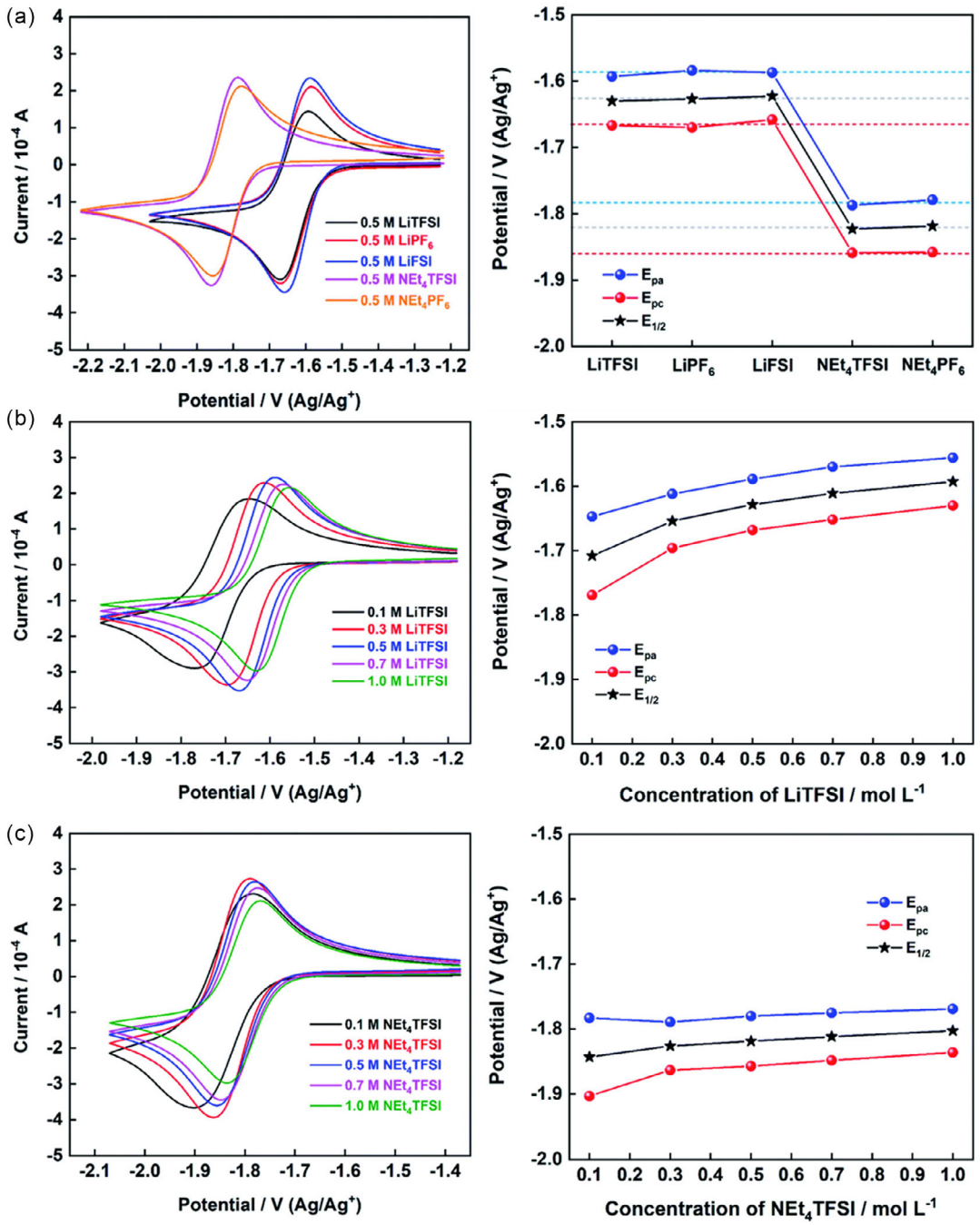

FIGURE 3 | (a) Cyclic voltammograms and corresponding redox potentials of BzNSN in various supporting electrolytes in CH_3CN. (b) Cyclic voltammograms and corresponding redox potentials of BzNSN in supporting electrolytes with various concentrations of LiTFSI in CH_3CN. (c) Cyclic voltammograms and corresponding redox potentials of BzNSN in supporting electrolytes with various concentrations of NEt_4TFSI in CH_3CN. The concentration of BzNSN is 10 mM, and the scan rate is 100 mV s^{-1}. Reproduced with permission [68]. Copyright 2020, Royal Society of Chemistry.

TABLE 1 | Common reference electrode potential conversion [54, 71, 72].

Reference electrode	Potential vs. SHE, V	Potential vs. Ag/Ag^+, V	Potential vs. Li/Li^+, V	Potential vs. Fc/Fc^+, V
SHE	N/A	−0.587	+2.841	−0.624
Ag/Ag^+	+0.587	N/A	+3.428	−0.037
Li/Li^+	−2.841	−3.428	N/A	−3.465
Fc/Fc^+	+0.624	+0.037	+3.465	N/A

etc. Yan et al. studied the lowest energy conformations of a series of cyclopropene radicals through DFT simulations and successfully developed a CP solubility prediction model using the calculated structural parameters [73]. Sanford et al. used DFT calculations to predict the redox potentials of various 1,2-bis(diisopropylamino)-3-cyclopropenyl-functionalized (DAC-functionalized) benzene derivatives and synthesized eight active molecules based on the calculations, successfully discovering a derivative that can achieve an optimal balance between redox potential and stability [74]. However, several of the molecules with the highest potentials are unstable, and there are still limitations in achieving both high stability and high potential.

3 | Redox Potential Regulation of Organic Cathode Materials

High-potential cathodes are crucial for advancing NAORFBs with high energy densities. This chapter will examine common organic cathode materials (p-type), such as ferrocene, phenothiazine, tetrathiafulvalene, TEMPO, and cyclopropyl cations, and will explore strategies for regulating their potential, providing both theoretical insights and practical guidance for designing high-potential cathodes. The redox potential data of these compounds are summarized in Table 2.

3.1 | Ferrocene

Ferrocene (Fc)-based materials, with their unique sandwich structure and reversible single-electron redox characteristics, have become a classic type of cathode for NAORFBs [93–95]. As a cathode, ferrocene was utilized as the redox core for one electron-transfer events (Figure 4a).

Figure 4a summarizes the structures of reported ferrocene derivatives used in NAORFBs. In 1992, Golovin et al. first used ferrocene and its derivatives as electrolyte additives in Li-ion batteries, owing to their key properties including high reversibility and fast

TABLE 2 | The performance summary of some typical cathode electrolyte materials in NAORFBs.

Cathode	$E_{1/2}$, V	Supporting electrolyte	Solubility	Cycling stability	Limiting failure mode	Ref
Fc	+3.25 vs. Li/Li^+	1.2 M LiTFSI/EC/PC/EMC	0.2 M	N/A	N/A	[75]
Fc-1	+3.47 vs. Li/Li^+	1.2 M LiTFSI/EC/PC/EMC	1.7 M	100	N/A	[75]
Fc-2	+3.45 vs. Li/Li^+	1.2 M $LiClO_4$/EC/PC/EMC	0.63 M	500	Mild self-discharge	[76]
Fc-3	+3.44 vs. Li/Li^+	1.2 M $LiBF_4$/EC/PC/EMC	1.71 M	500	Precipitation of oxidized ferrocenium	[76]
Fc-4	+3.49 vs. Li/Li^+	1.2 M $LiPF_4$/EC/PC/EMC	0.40 M	<10	Precipitation of oxidized ferrocenium	[76]
Fc-5	+0.22 vs. Ag/Ag^+	1 M $TEAPF_6$/ACN	0.5 M	N/A	N/A	[77]
Fc-6	+3.1 vs. Li/Li^+	1 M LiTFSI EC/DEC	0.1 M	50	N/A	[77]
Fc-7	+3.15 vs. Li/Li^+	1.0 M $LiClO_4$/EC/DEC	>0.05 M	1000	N/A	[78]
Fc-8	+3.55 vs. Li/Li^+	1 M $LiPF_6$/DMC:EC	0.20 M	N/A	N/A	[79]
Fc-9	+3.65 vs. Li/Li^+	1 M $LiPF_6$/PC	0.81 M	400	Redox-active species crossover	[80]
PTZ-1	+0.289 vs. Fc/Fc^+ +0.928 vs. Fc/Fc^+	1 M LiTFSI/PC	0.42 M	50	Dication instability	[81]
PTZ-2	+0.174 vs. Fc/Fc^+ +0.824 vs. Fc/Fc^+	1 M LiTFSI/PC	0.15 M	50	Dication instability	[81]
PTZ-3	+0.068 vs. Fc/Fc^+ +0.632 vs. Fc/Fc^+	1 M LiTFSI/PC	0.10 M	50	Dication instability	[81]
PTZ-4	+0.311 vs. Fc/Fc^+ +0.937 vs. Fc/Fc^+	0.5 M TEATFSI/ACN	0.4 M	N/A	N/A	[82]
PTZ-5	+0.093 vs. Fc/Fc^+ +0.666 vs. Fc/Fc^+	0.5 M TEATFSI/ACN	0.11 M	N/A	N/A	[82]
PTZ-6	+0.064 vs. Fc/Fc^+ +0.654 vs. Fc/Fc^+	0.5 M TEATFSI/ACN	0.55 M	140	Active species crossover	[82]
PTZ-7	+0.64 vs. Fc/Fc^+ +1.00 vs. Fc/Fc^+	0.5 M $TBAPF_6$/ACN	N/A	100	Dication solubility limitation	[66]

(Continues)

TABLE 2 | (Continued)

Cathode	$E_{1/2}$, V	Supporting electrolyte	Solubility	Cycling stability	Limiting failure mode	Ref
TEMPO-1	+3.5 vs. Li/Li^+	1.0 M $LiPF_6$/PC/EC/EMC	N/A	100	High concentrations	[83]
TEMPO-2	+3.49 vs. Li/Li^+	1 M $LiPF_6$/PC	>0.05 M	50	Radical instability of unsubstituted TEMPO	[84]
TEMPO-3	+3.63 vs. Li/Li^+	1 M $LiBF_4$/PC	0.5 M	100	High ohmic resistance	[85]
TEMPO-4	+0.39 vs. Ag/Ag^+	0.5 M LiTFSI/ACN	N/A	100	N/A	[86]
TEMPO-5	+0.40 vs. Ag/Ag^+	0.5 M LiTFSI/ACN	N/A	N/A	N/A	[86]
TEMPO-6	+0.40 vs. Ag/Ag^+	0.5 M LiTFSI/ACN	N/A	N/A	N/A	[86]
TTF-1	−0.04 vs. Fc/Fc^+ +0.34 vs. Fc/Fc^+	EC/DMC	0.25 M	150	Redox species crossover and minor membrane degradation	[87]
TTF-2	−0.02 vs. Fc/Fc^+ +0.34 vs. Fc/Fc^+	N/A	N/A	150	Redox species crossover and minor membrane degradation	[87]
TTF-3	+0.09 vs. Fc/Fc^+ +0.48 vs. Fc/Fc^+	N/A	0.17 M	150	Redox species crossover and minor membrane degradation	[87]
TTF-4	+0.09 vs. Fc/Fc^+ +0.48 vs. Fc/Fc^+	N/A	N/A	150	Redox species crossover and minor membrane degradation	[87]
TTF-5	+3.43 vs. Li/Li^+ +3.78 vs. Li/Li^+	EC/DMC	0.02 M	100	Redox species crossover	[88]
TTF-6	+3.60 vs. Li/Li^+ +3.91 vs. Li/Li^+	EC/DMC	0.03 M	100	Redox species crossover	[88]
TTF-7	+3.58 vs. Li/Li^+ +3.90 vs. Li/Li^+	EC/DMC	0.20 M	100	Redox species crossover	[88]
TTF-8	+0.40 vs. Ag/Ag^+ +0.71 vs. Ag/Ag^+	0.1 M/PC/$TBAPF_6$/ACN	<0.20 M	400	N/A	[89]
TTF-9	+0.21 vs. Ag/Ag^+ +0.47 vs. Ag/Ag^+	0.1 M/PC/$TBAPF_6$/ACN	<0.35 M	100	N/A	[89]
TTF-10	+0.18 vs. Ag/Ag^+ +0.43 vs. Ag/Ag^+	0.1 M/PC/$TBAPF_6$/ACN	0.5 M	100	N/A	[89]
TTF-11	+0.70 vs. Ag/Ag^+ +1.01 vs. Ag/Ag^+	0.1 M $LiPF_6$/EC/EMC	0.01 M	100	N/A	[90]
TTF-12	+0.43 vs. Ag/Ag^+ +0.65 vs. Ag/Ag^+	0.1 M $LiPF_6$/EC/EMC	0.75 M	100	N/A	[90]
CP-1	+0.98 vs. Fc/Fc^+	0.5 M $LiPF_6$/ACN	>1 M	10	Molecular decomposition	[91]
CP-2	+0.98 vs. Fc/Fc^+	0.5 M $LiPF_6$/ACN	>1 M	10	Molecular decomposition	[91]
CP-3	+0.83 vs. Fc/Fc^+	0.5 M $LiPF_6$/ACN	>1 M	125	N/A	[91]
CP-4	+0.82 vs. Fc/Fc^+	0.5 M $LiPF_6$/ACN	1.7 M	200	Sensitivity to water	[91]
CP-5	+0.84 vs. Fc/Fc+	0.5 M $LiPF_6$/ACN	1.5 M	200	Low solubility of charged radical dication	[91]
CP-6	+1.40 vs. Fc/Fc^+	0.5 M $TBAPF_6$ in ACN	N/A	N/A	Molecular decomposition	[92]
CP-7	+1.35 vs. Fc/Fc^+	0.5 M $TBAPF_6$ in ACN	N/A	30	Molecular decomposition	[92]
CP-8	+1.36 vs. Fc/Fc^+	0.5 M $TBAPF_6$ in ACN	N/A	60	Molecular decomposition	[92]
CP-9	+1.33 vs. Fc/Fc^+	0.5 M $TBAPF_6$ in ACN	>0.2 M	150	Minimal decomposition	[92]
CP-10	+1.60 vs. Fc/Fc^+	0.5 M KPF_6/ACN	N/A	N/A	DAC–arene derivative instability	[73]

(Continues)

TABLE 2 | (Continued)

Cathode	$E_{1/2}$, V	Supporting electrolyte	Solubility	Cycling stability	Limiting failure mode	Ref
CP-11	+1.51 vs. Fc/Fc^+	0.5 M KPF_6/ACN	N/A	N/A	DAC–arene derivative instability	[73]
CP-12	+1.31 vs. Fc/Fc^+	0.5 M KPF_6/ACN	N/A	150	DAC–arene derivative instability	[73]
CP-13	+1.19 vs. Fc/Fc^+	N/A	N/A	N/A	DAC–arene derivative instability	[73]

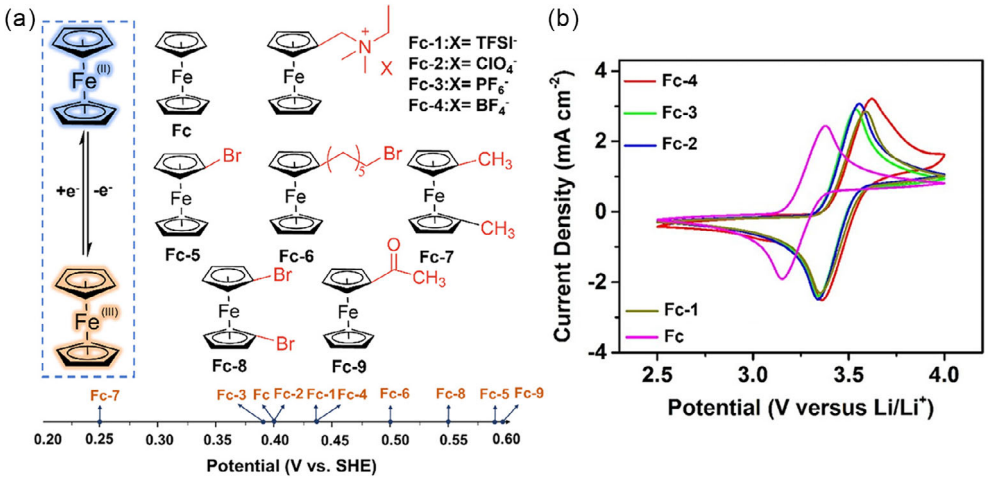

FIGURE 4 | (a) Scheme of the redox process of the ferrocene core, structures of selected ferrocene derivatives, and their potential axis distribution. (b) CV curves of 0.05 M Ionic-Fcs and pristine Fc in 1.2 M LiA supporting electrolytes in EC/PC/EMC (4:1:5 by wt.) at a scan rate of 50 mV s^{-1}. Reproduced with permission [76]. Copyright 2015, Springer Nature.

kinetics [72]. Due to its low solubility, the direct use of ferrocene as a redox-active species in RFBs falls far short of the practical requirements for such systems. In 2015, Wang et al. designed a positively charged tetraalkylammonium group and paired it with a $TFSI^-$ counter anion for NAORFBs. The compound exhibited a redox potential of +3.49 V vs. Li/Li^+, which is 0.23 V higher than pristine ferrocene (+3.26 V vs. Li/Li^+) due to the electron-withdrawing ammonium pendant. This modification enabled a high cell voltage of 3.5 V in a Li-organic hybrid flow battery [75]. The same group further investigated the effects of various counter anions on the properties of ionic functionalized ferrocenes for NAORFBs. They reported that the redox potentials of the ionic ferrocene derivatives (**Fc-1–Fc-4**) were consistently shifted to approximately +3.44 to +3.49 V vs. Li/Li^+ (Figure 4a). The specific redox potentials were +3.49 V vs. Li/Li^+ for BF_4^-, +3.47 V vs. Li/Li^+ for $TFSI^-$, +3.45 V vs. Li/Li^+ for ClO_4^-, and +3.44 V vs. Li/Li^+ for PF_6^-, demonstrating that the counter anion had a minor influence (Figure 4b) [76]. Kim et al. systematically tuned the cell voltage of NAORFBs by pairing substituted ferrocene and cobaltocene derivatives. They demonstrated that introducing an electron-withdrawing bromo group to ferrocene (**Fc-5**) raised its redox potential by 0.178 V [77]. Park et al. developed **Fc-6** as the cathode, demonstrating that functionalization of ferrocene with a bromohexyl chain can significantly enhance its solubility in common organic electrolytes, while maintaining excellent electrochemical stability [96]. In 2017, Lu et al. utilized a low-melting-point ferrocene derivative **Fc-7**, as a neat liquid cathode for a NAORFB. The redox potential of **Fc-7** was measured to be slightly lower than that of pristine ferrocene due to the electron-donating effect of the methyl groups [78]. Wang and coworkers designed a $LiFePO_4$-based semiliquid RFB using **Fc** and **Fc-8** as redox mediators. The redox potential of ferrocene is +3.25 V vs. Li/Li^+, which increases to +3.55 V vs. Li/Li^+ upon introducing two bromine substituents [79]. In addition, Oh et al. simultaneously tuned the solubility and redox potential by employing acetyl ferrocene (**Fc-9**) as the cathode active material [80]. Due to the electron-withdrawing effect of the acetyl group, the redox potential of ferrocene is raised to +3.65 V vs. Li/Li^+.

3.2 | Phenothiazine

Phenothiazine (PTZ) derivatives is a class of sulfur-containing nitrogen heterocyclic compounds with a unique tricyclic conjugated framework. This structural feature endows it with inherently tunable redox-active centers, making it one of the promising cathode candidates in the field of NAORFBs. In practical application, the redox potential of phenothiazine usually ranges from +2.5 to +3.0 V vs. Li/Li^+. While it possesses basic redox activity, it still falls short of the requirements for high-voltage NAORFBs. Therefore, focusing on structural modification of phenothiazine to enhance their potential while balancing cycling stability and electrolyte compatibility has become a key research direction in the field of NAORFBs in recent years [97–99].

A straightforward and often-used strategy is to place EDGs or EWGs on the phenothiazine aromatic framework. Figure 5a

summarizes representative phenothiazine-based compounds used in NAORFBs. To stabilize the redox process of the second electron, in 2017, Odom et al. lowered the first oxidation potential to +0.068 V vs. Fc/Fc^+ by introducing electron-donating methoxy groups at the para positions of the nitrogen atom. By contrast, the first oxidation potential of the parent compound **PTZ-1** was +0.289 V vs. Fc/Fc^+, and that of the dimethyl analog **PTZ-2** was +0.174 V vs. Fc/Fc^+. This substitution strategy, which enables extensive charge delocalization, stabilized the second oxidation state, rendering its redox potential at +0.632 V vs. Fc/Fc+ electrochemically reversible (Figure 5b). Figure 5c shows the cycling profiles for each of the bulk electrolysis experiments [81]. In 2019, Attanayake et al. developed two new phenothiazine derivatives, **PTZ-5** and **PTZ-6**. By introducing electron-donating oligoglycol chains at different positions on the phenothiazine core, they systematically tuned the redox potentials. The first oxidation potentials were precisely adjusted to +0.093 and +0.064 V vs. Fc/Fc^+ for **PTZ-5** and **PTZ-6**, respectively, while maintaining reversible second oxidations at +0.666 and +0.654 V vs. Fc/Fc^+. Figure 5d shows the first and second oxidation events of **PTZ-1**, **PTZ-3**, **PTZ-4**, **PTZ-5**, and **PTZ-6**. They systematically varied the substituents to investigate the resulting tradeoffs in solubility,

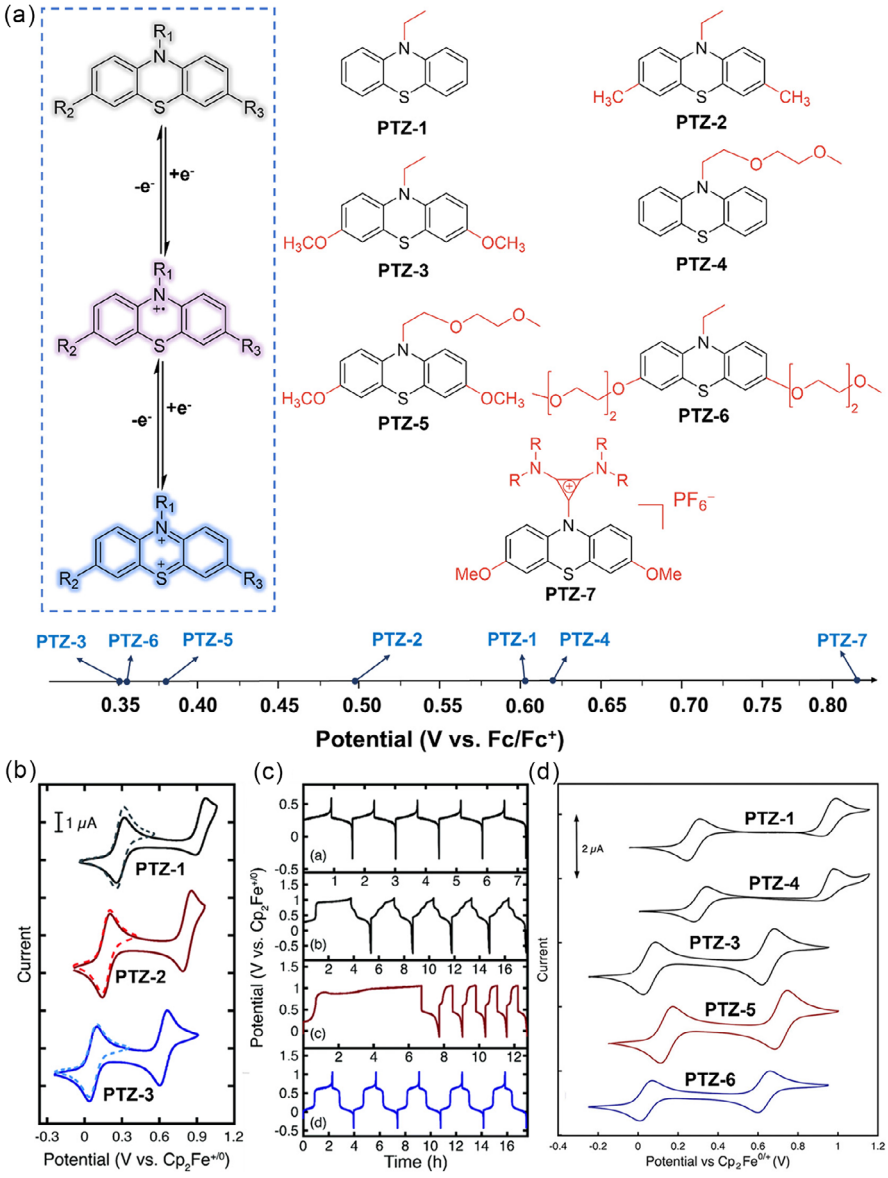

FIGURE 5 | (a) Scheme of the redox process of the phenothiazine core, structures of selected phenothiazine derivatives, and their potential axis distribution. (b) Cyclic voltammograms of the first and second oxidations of 1 mM PTZ-1, PTZ-2, and PTZ-3 in 1 M LiTFSI in PC. Reproduced with permission [81]. Copyright 2017, Royal Society of Chemistry. (c) At 1 mM active material in 1 M LiTFSI/PC and 0.804 mA constant current, the first five galvanostatic charge/discharge potential profiles are shown from top to bottom: first oxidation of PTZ-1, first and second oxidations of PTZ-1, first and second oxidations of PTZ-2, and first and second oxidations of PTZ-3. Reproduced with permission [81]. Copyright 2017, Royal Society of Chemistry. (d) Cyclic voltammograms showing the first and second oxidation events of PTZ-1, PTZ-3, PTZ-4, PTZ-5, and PTZ-6 at 1 mM in 0.5 M TEATFSI in ACN at a scan rate of 10 mV s^{-1}. Reproduced with permission [82]. Copyright 2019, American Chemical Society.

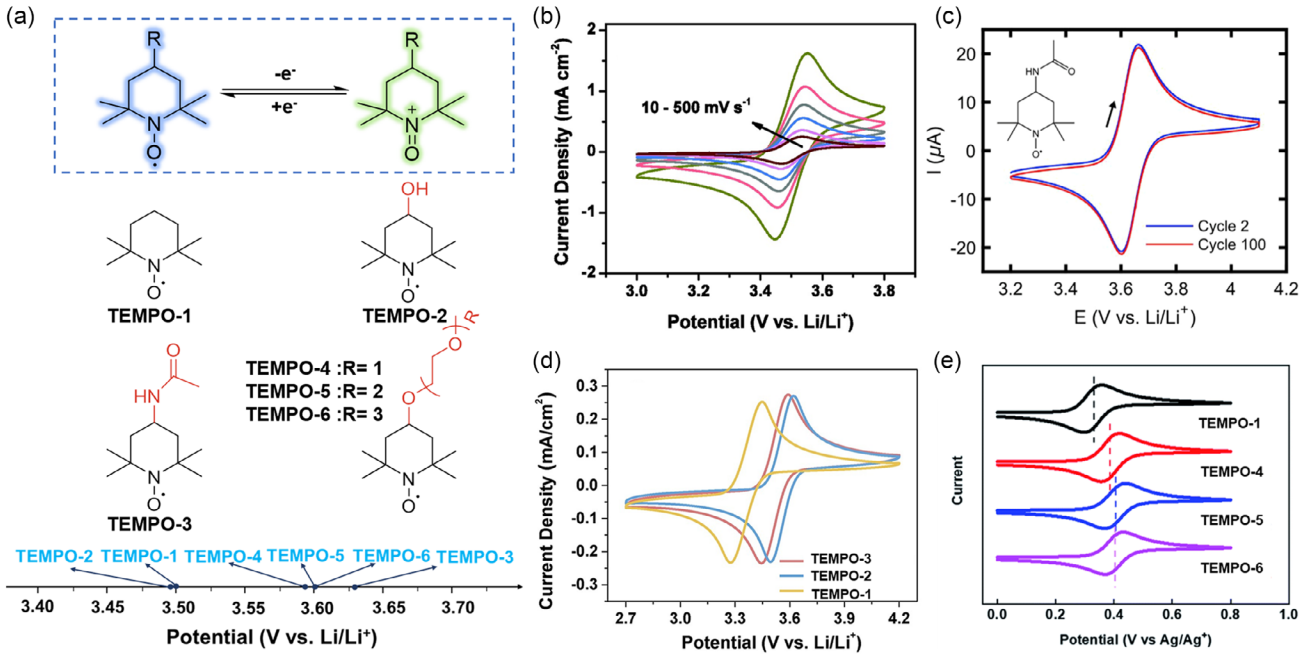

FIGURE 6 | (a) Scheme of the redox process of the TEMPO core, structures of selected TEMPO derivatives, and their potential axis distribution. (b) CV curves of 0.005 M TEMPO in 1.0 M $LiPF_6$ on a glassy carbon electrode at scan rates ranging from 10–500 mV s^{-1}. Reproduced with permission [83]. Copyright 2014, John Wiley and Sons. (c) CV cycling over 100 cycles (at 100 mV s^{-1}) for TEMPO-3. Reproduced with permission [85]. Copyright 2016, Elsevier. (d) CV curves of TEMPO derivatives before charge/discharge on a platinum wire electrode vs. Li/Li^+ at a scan rate of 50 mV s^{-1}. Reproduced with permission [84]. Copyright 2019, Elsevier. (e) CV curves of 10 mM TEMPO-based redoxmers (ACN/0.5 M LiTFSI, 100 mV/s^{-1}). Reproduced with permission [86]. Copyright 2021, Royal Society of Chemistry.

reaction kinetics, and redox potentials [82]. In 2021, Sanford et al. introduced a DAC-PTZ hybrid architecture, enabling simultaneous optimization of redox potential, solubility, and reversibility. In their design, they replaced the conventional C–C coupling between DAC and PTZ by a modular C–N linkage, which greatly simplifies synthetic access and allows a broader array of substituent variation. This modular platform enables one to adjust the steric and electronic coupling between the DAC acceptor and the PTZ donor. The DAC moiety, being strongly π-accepting, interacts with the PTZ HOMO and draws electron density in the oxidized states, thereby stabilizing high oxidation levels and raising redox potentials. From their structure–property exploration, the optimized compound named **PTZ-7** displayed two fully reversible oxidation events at +0.64 and +1.00 V vs. Fc/Fc^+, corresponding to a high potential span when paired with a suitable anode [66].

3.3 | TEMPO

2,2,6,6-tetramethylpiperidine-1-oxyl (TEMPO) is a typical type of heterocyclic organic molecule containing nitroxide free radicals (Figure 6a). Owing to the conjugated delocalization property of unpaired electrons on the N–O bond and the steric hindrance effect of four methyl groups on adjacent carbon atoms, it possesses both excellent reversibility of redox reactions and stability of free radicals, thus becoming a research focus as a cathode material for NAORFBs.

In 2014, Wang et al. reported that the solubility of **TEMPO-1** in the mixed solvent of ethylene carbonate (EC)/propylene carbonate (PC)/ethyl methyl carbonate (EMC) (with a weight ratio of 4:1:5) reaches 5.2 M. As shown in Figure 6b, **TEMPO-1** displays well-defined redox peaks in the potential range of 2.5–4.0 V at scan rates ranging from 10 to 500 mV s^{-1}. In the 1.0 M $LiPF_6$/EC-PC-EMC system, the redox potential of **TEMPO-1** reaches +3.5 V vs. Li/Li^+ [83].

In 2016, Brushett et al. introduced an acetamido ($-NHCOCH_3$) substituent at the 4-position of the piperidine ring, obtaining the derivative **TEMPO-3** [85]. This substituent regulates the electron cloud density of the piperidine ring and the N–O active site through conjugation effect and inductive effect. The nitrogen atom in the acetamido group forms a conjugated system with the carbonyl group (C=O), and its electronic effect changes the delocalization degree of unpaired electrons on the N–O bond, thereby affecting the energy barrier of the redox reaction and causing the redox potential to shift positively to +3.63 V vs. Li/Li^+ (Figure 6c). In 2019, Koo et al. synthesized two derivatives, namely, **TEMPO-2** and **TEMPO-3**, by introducing substituents with different polarity and electron-withdrawing properties ($-OH$, $-NHCOCH_3$) at the 4-position of the piperidine ring [84]. As shown in Figure 6d, **TEMPO-2** and **TEMPO-3** experienced a highly reversible redox reaction under load conditions with improved long-term stability when compared to **TEMPO-1**. The positive shift of the potential originated from the electron-withdrawing effect of the substituents, the $-OH$ and $-NHCOCH_3$ weakened the electron cloud density of the N–O bond through the inductive effect.

In 2021, Zhang et al. introduced polyethylene glycol (PEG) chains with different lengths onto the hydroxyl group at the

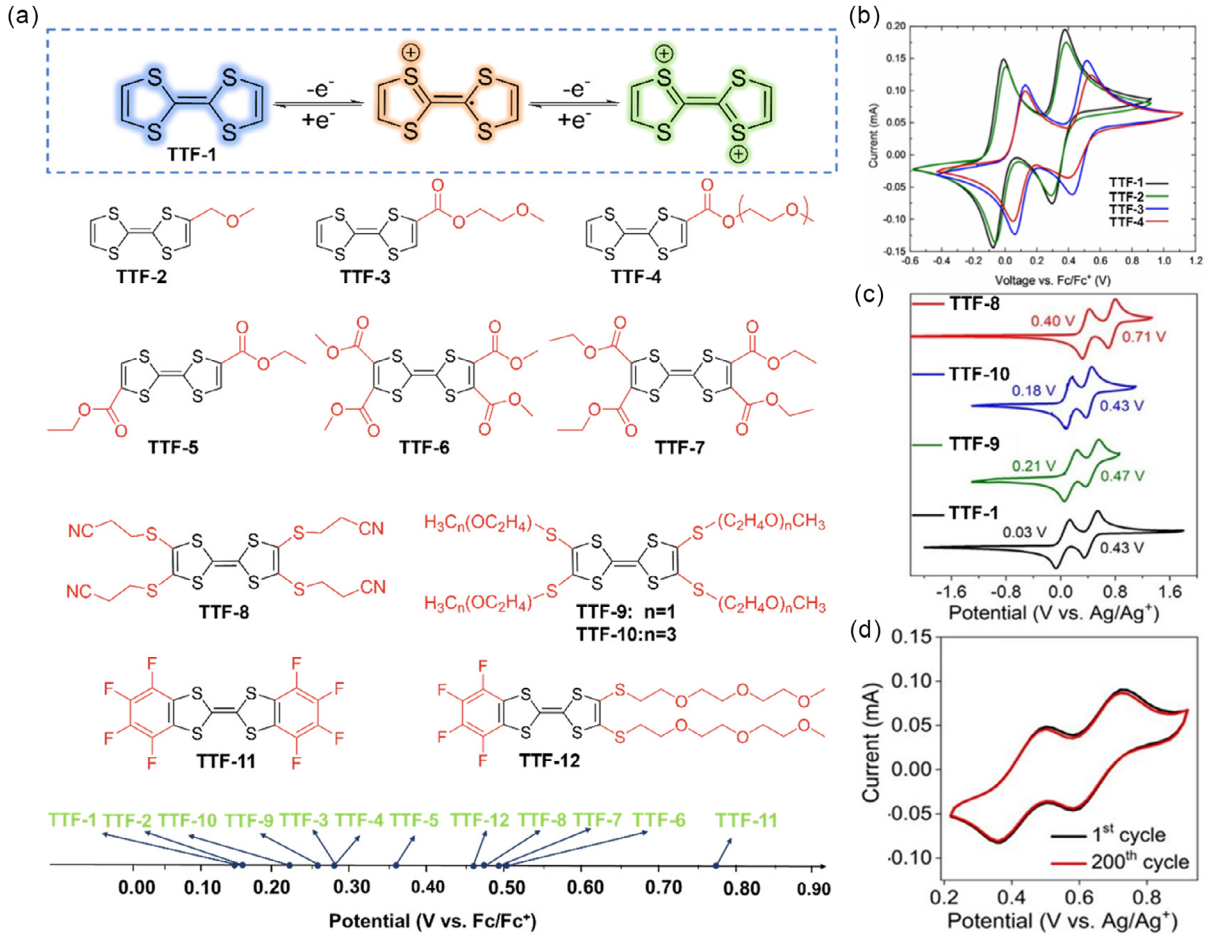

FIGURE 7 | (a) Scheme of the redox process of the TTF core, structures of selected TTF derivatives, and their potential axis distribution. (b) CV curves of TTF1–4 (5 mM in acetonitrile containing 200 mM $TBAPF_6$) recorded with a scan rate of 100 mV s^{-1}. Reproduced with permission [87]. Copyright 2022, John Wiley and Sons. (c) CV curves of TTF-1, TTF-8, TTF-9, and TTF-10 for 1 mM solutions in 0.1 M $TBAPF_6$/MeCN at a scan rate of 50 mV s^{-1}. Reproduced with permission [89]. Copyright 2023, Royal Society of Chemistry. (d) CV curves of TTF-12. Reproduced with permission [90]. Copyright 2024, John Wiley and Sons.

4-position of the piperidine ring via the Williamson ether coupling reaction [86]. This modification achieved a physical state transition from solid to liquid, and the resulting derivatives were fully miscible with CH_3CN, leading to a significant improvement in solubility. Meanwhile, cyclic voltammetry tests showed that in 0.5 M LiTFSI/CH_3CN, the redox potential of pure **TEMPO-1** was +0.33 V vs. Ag/Ag^+, while the potential of **TEMPO-4** shifted positively by approximately 60 mV to +0.39 V vs. Ag/Ag^+, that of **TEMPO-5** shifted slightly further positively to +0.40 V vs. Ag/Ag^+, and that of **TEMPO-6** remained at +0.40 V (Figure 6e). All of this stems from the fact that the oxygen atoms on the PEG chain reduce the electron cloud density on the TEMPO ring via the electron-withdrawing inductive effect. Furthermore, the longer the PEG chain, the more obvious the molecular folding conformation, and the amplitude of the positive potential shift gradually slowed down.

3.4 | Tetrathiafulvalene

Tetrathiafulvalene (TTF) is a class of classic organic electronic donor molecules composed of two 1,3-dithiolate-substituted cyclopentene units (Figure 7a). Its core advantage lies in possessing two-step reversible single-electron redox properties, which sequentially lose electrons to generate stable radical cations (TTF^+) and dications (TTF^{2+}) [100]. The multielectron reaction mechanism of TTF, which significantly enhances the charge storage capacity per unit volume, helps overcome the energy density limitations of single-electron materials and meets the core demand for high volumetric capacity cathode in NAORFBs.

In 2022, Janssen et al. synthesized three TTF derivatives that solved the solubility issue of TTF and achieved redox potential regulation. **TTF-1** is the unmodified TTF parent molecule, served as a reference for potential regulation in the study; in a 0.2 M $TBAPF_6$/MeCN solution, its two-step oxidation potentials were −0.04 and + 0.34 V vs. Fc/Fc^+ (Figure 7b) [87]. To simultaneously improve the redox potential and solubility, the authors lithiate TTF and then quench it with the corresponding acyl chloride to synthesize **TTF-3** and **TTF-4**. **TTF-3** is a solid with a solubility of 0.17 ± 0.01 M in acetonitrile, while **TTF-4** is a liquid at room temperature and fully miscible with acetonitrile, with a molar concentration of 3.8 ± 0.2 M. Compared to **TTF-1** and **TTF-2**, **TTF-3** and **TTF-4** exhibited a 0.11–0.14 V positive shift in their redox potentials. This positive shift is attributed to the strong electron-withdrawing effect of the carbonyl (C=O) group in

the ester, which lowers the electron density of the TTF parent molecule through both inductive and π–π conjugation effects.

In 2022, Chen et al. synthesized **TTF-5**, **TTF-6**, and **TTF-7** and explored the regulation of organic molecule potentials by varying the number of ester groups and alkyl chain lengths. By introducing a pair of ethyl ester groups (–COOEt) into the TTF core, TTFDE achieved an increase in the redox potential via the electron-withdrawing inductive effect of the ester group. The CV curve of **TTF-5** exhibited two pairs of oxidation/reduction peaks, with oxidation potentials at +3.62 and +3.97 V vs. Li/Li^+, and reduction potentials at +3.24 and +3.59 V vs. Li/Li^+ in 1 M $LiPF_6$/EC-DEC (1:1, v/v), representing a potential increase compared to unmodified TTF. **TTF-6** further increased the number of EWGs by introducing two pairs of methyl ester groups (–COOMe) symmetrically on both sides of the TTF core. CV tests revealed that the oxidation potentials of **TTF-6** were raised to +3.75 and +4.01 V vs. Li/Li^+, and the reduction potentials were +3.45 and +3.81 V vs. Li/Li^+, showing an increase compared to **TTF-5**. Compared to the two ester group in **TTF-5**, the four ester groups in **TTF-6** more deeply lower the HOMO energy level of the TTF core through the dual electron-withdrawing effect, further increasing the energy barrier for oxidation and directly resulting in an increase in the oxidation potential. Building on **TTF-6**, **TTF-7** replaced the methyl ester groups (–COOMe) with ethyl ester groups (–COOEt), achieving both high potential and enhanced stability. CV test showed that TTFTE had oxidation potentials of +3.63 and +3.93 V vs. Li/Li^+ and reduction potentials of +3.52 and +3.86 V vs. i/Li^+. The carbonyl groups of the ethyl ester still maintained a strong electron-withdrawing capability, allowing **TTF-6** to retain its high potential characteristics. More importantly, at a 0.5 C rate, when using 0.2 M **TTF-7** as the cathode and QA-Radel anion-exchange membrane as the separator, the battery showed a discharge potential platform decay rate of only 5% after 100 cycles, with a stable Coulombic efficiency of over 91.09%, significantly outperforming **TTF-5** and **TTF-6** [88].

In 2023, Jiang et al. designed two series of derivatives, **TTF-8**, **TTF-9**, and **TTF-10**. **TTF-8** introduces cyanethyl chains ($-CH_2CH_2CN$) at four active sites of the TTF core. This modification leverages both the strong electron-withdrawing properties of the cyano group and the steric hindrance effect of the ethyl chain to regulate the potential. Its two-step single-electron redox potentials are +0.40 and +0.71 V vs. Ag/Ag^+, significantly shifted in the positive direction compared to unmodified TTF (+0.03 and +0.43 V vs. Ag/Ag^+ in 0.1 M $TBAPF_6$/MeCN), with a shift exceeding 0.3 V. The core reason lies in the strong electron-withdrawing effect of the cyano group, which pulls electron density from the TTF core's conjugated system via the ethyl chain, lowering the electron density and increasing the energy barrier for oxidation reactions, leading to a higher redox potential. **TTF-9** and **TTF-10** involve grafting PEG chains with varying polymerization degrees onto the TTF core. The weak electron-withdrawing effect of the PEG chain and its affinity for solvents allow for fine-tuning of the potential. For **TTF-9**, the two redox potentials are +0.21 and +0.47 V vs. Ag/Ag^+ in 0.1 M $TBAPF_6$/MeCN, which represent a positive shift of 0.18 and 0.04 V compared to the original TTF (+0.03 and +0.43 V vs. Ag/Ag^+). The short PEG chain has a minimal spatial hindrance, allowing a more direct electron-withdrawing effect from the oxygen atom. For **TTF-10**, the redox potentials in the same system are +0.18 and +0.43 V vs. Ag/Ag^+, showing a smaller shift (0.15 and 0 V), which is attributed to the increased spatial hindrance from the longer PEG chain, slightly reducing the efficiency of the electron-withdrawing effect from the oxygen atoms to the TTF core (Figure 7c) [89]. In 2024, Jiang et al. synthesized **TTF-11** and **TTF-12** by modifying with symmetric and asymmetric strong EWGs. **TTF-11** directly fuses two perfluorophenyl groups (PerF) onto the TTF-conjugated backbone, leveraging the strong electron-withdrawing effect of the symmetric double substitution to significantly increase the potential [87]. Its redox potentials are +0.70 and +1.01 V vs. Ag/Ag^+, which are significantly positively shifted compared to the reference **TTF-10**. The core reason for this shift lies in the multiple highly electronegative fluorine atoms in the PerF group, which, through π-conjugation, integrate into the TTF's π-electronic framework, directly lowering the electron density of the TTF core, thereby resulting in a large positive potential shift. However, the symmetric fused structure leads to high molecular coplanarity and easy aggregation, which, although not affecting the potential characteristics, results in very low solubility (<0.01 M). **TTF-12** achieves a balance of potential and solubility by asymmetric substitution of the TTF core, with one side bearing a perfluorophenyl group (PerF) and the other side bearing a PEG3 chain. The strong electron-withdrawing PerF group and the weakly polar PEG3 chain synergistically optimize both potential and solubility. In a 0.1 M $LiPF_6$/EC/EMC (1:1) electrolyte at a 50 mV/s scan rate, the two redox potentials of **TTF-12** are +0.43 and +0.65 V vs. Ag/Ag^+, which are positive shifts of 0.25 and 0.22 V compared to **TTF-10** (+0.18 and +0.43 V vs. Ag/Ag^+). The PEG3 chain is primarily used to enhance solubility and suppress membrane penetration, without interfering with the electronic effect transmission.

3.5 | Cyclopropenium

Cyclopropenium cation-based materials represent an emerging class of high-potential organic cathodes whose core advantage lies in their inherent cationic nature (Figure 8a). The energy storage active center is the tricyclic cyclopropenium cation (CP^+), which operates via a reversible one-electron oxidation reaction CP^+/CP^{2+}, where CP^{2+} exists as a radical dication [91].

In 2017, Sanford et al. first reported the use of cyclopropenium cation (CP^+) derivatives as catholyte for NAORFBs. By designing five hexafluorophosphate compounds (**CP-1–CP-5**), they investigated the mechanism of redox potential regulation through nitrogen atom substitutions. As shown in Figure 8b, all five molecules exhibited chemically reversible redox couples. **CP-1** and **CP-2** are cyclopropenium derivatives with mixed phenyl and alkyl substitutions, while **CP-3**, **CP-4**, and **CP-5** are fully alkyl-substituted. Due to the similar electron-donating abilities of methyl and ethyl, the redox potentials of **CP-1** and **CP-2** are both +0.98 V vs. Fc/Fc^+. However, the electron-withdrawing conjugation of the phenyl with the cyclopropenium ring significantly lowers the electron cloud density of the ring, resulting in a much higher potential (by 150 mV) compared to **CP-3,4,5**. Furthermore, since the electron-donating abilities of methyl and ethyl groups are similar, and the steric hindrance of isopropyl only slightly adjusts the electron cloud, the potential differences among the three compounds are minimal [91].

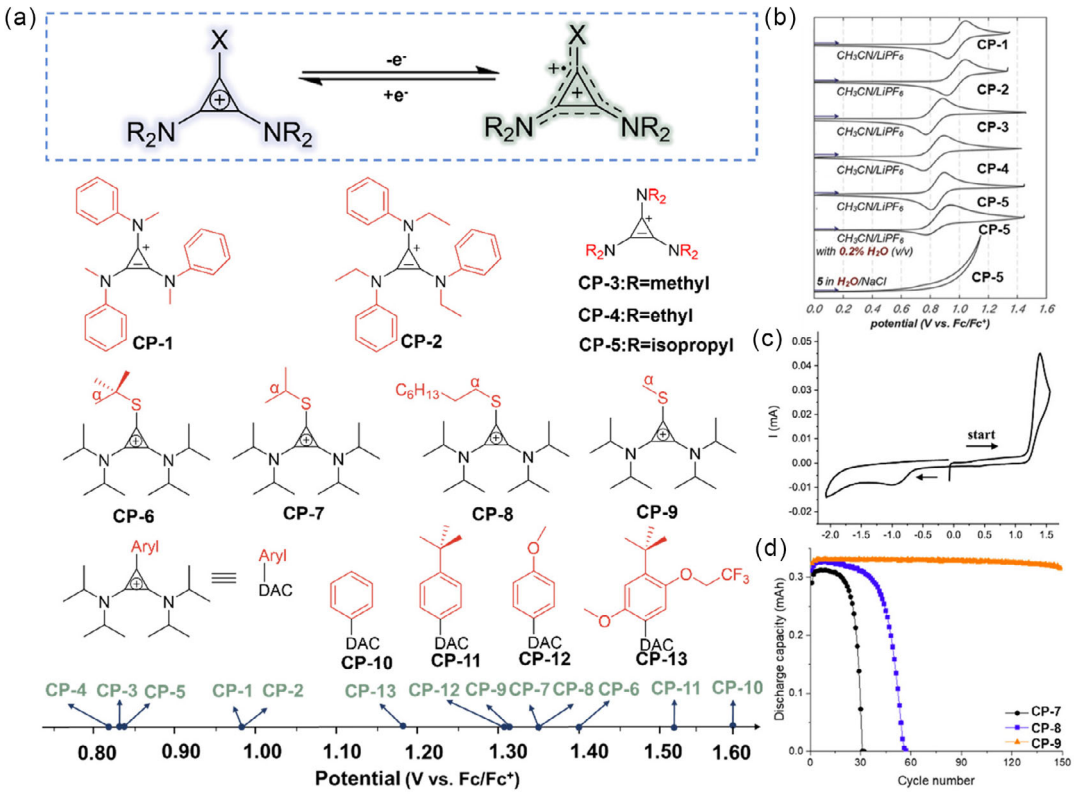

FIGURE 8 | (a) Scheme of the redox process of the cyclopropenium core, structures of selected cyclopropenium derivatives, and their potential axis distribution. (b) CV of 1–5 as 5×10^{-3} M solutions under the specified conditions at 100 mV s^{-1}. Reproduced with permission [91]. Copyright 2016, John Wiley and Sons. (c) CV of CP-6 (5 mM in 0.5 M $TBAPF_6$/MeCN with a glassy carbon working electrode. Reproduced with permission [92]. Copyright 2019, American Chemical Society. (d) Capacity versus cycle number for bulk electrolysis cycling of CP-7, CP-8, and CP-9 (5 mM in 0.5 M $TBAPF_6$/MeCN). Reproduced with permission [92]. Copyright 2019, American Chemical Society.

To overcome the potential limitation, Sanford et al. introduced a heteroatom substitution strategy involving the weak π-donating sulfur atom in place of the strong π-donating nitrogen atom. This modification resulted in a significant increase in the redox potential of sulfur-substituted cyclopropenium derivatives (+1.33 to +1.36 V vs. Fc/Fc^+), with an improvement of approximately 470 mV compared to the nitrogen-containing precursor (**CP-4**, +0.86 V vs. Fc/Fc^+). The electron-donating ability of sulfur is weaker than that of nitrogen, which lowers the HOMO energy, making oxidation more difficult, thereby increasing the redox potential. However, the stability of the sulfur-substituted cyclopropenium derivatives is compromised by the C–S bond cleavage, leading to irreversible redox reactions (**CP-6**, Figure 8c). To address this issue, they synthesized **CP-7**, **CP-8**, and **CP-9** through the synergistic effect of the steric and electronic effects of alkyl substituents, optimizing stability while maintaining high potential. Since **CP-9** lacks β-H and its carbocation is the most unstable, the cleavage rate of the C–S bond is the slowest. As a result, it not only retained a high potential of +1.33 V vs. Fc/Fc^+ but also achieved high stability. In experiments, 2-Me^+ remained stable for 150 cycles under standard cycling conditions (Figure 8d) [92].

In 2020, Sanford et al. proposed an aromatic (aryl) substitution strategy for alkyl sulfide, leading to the development of the bis(diisopropylamino) aryl cyclopropenium ion. The electronic effects of the aryl group and alkyl sulfide are similar, preserving the high redox potential, while the aromatic ring lacks the easily cleaved C–S bond, ensuring stability. Furthermore, the aromatic ring allows for fine-tuning of the electronic effects and steric hindrance through substituents, further optimizing the balance between potential and stability. They synthesized a series of DAC-aromatic derivatives (**CP-10–CP-13**, Figure 8a) [73]. Due to the electron delocalization of the aromatic ring and conjugation with the tricyclic ring, it exhibits a high redox potential of +1.60 V vs. Fc/Fc^+, but the oxidation process is irreversible (no reduction peak). The redox process of **CP-11** is reversible with a potential of +1.51 V vs. Fc/Fc^+; however, the steric hindrance of the tert-butyl group fails to fully address the stability issue of the oxidized state. For **CP-12**, the introduction of the electron-donating methoxy group increases the electron cloud density of the aromatic ring, leading to a decrease in oxidation potential to +1.31 V vs. Fc/Fc^+. Subsequently, they synthesized compound **CP-13** by simultaneously introducing the methoxy, pentafluoropropoxy, and tert-butyl group. Through the precise synergy of EDGs, EWGs, and steric hindrance, it not only maintains a high potential of +1.19 V vs. Fc/Fc^+ but also achieves a capacity retention rate of 92% after 116 h of cycling in a 0.3 M symmetric flow battery, making it the optimal derivative with both high potential and high stability.

Beyond p-type catholytes, n-type organic materials also represent a particularly promising frontier for NAORFBs. Recent advances in strongly electron-deficient frameworks, such as conjugated sulfonamides, triflimide-functionalized aromatics, and cyanamide derivatives, have demonstrated redox potentials approaching

~4.0 V vs. Li/Li^+ (~0.7 V vs. Fc/Fc^+, depending on electrolyte conditions) in lithium-based systems [101, 102]. These elevated potentials arise from the incorporation of powerful EWGs, which substantially lower LUMO energy levels and stabilize the reduced species. Importantly, many of these compounds also exhibit appreciable solubility in polar aprotic media, an intrinsic limitation for solid-state batteries but a potential advantage for flow configurations. Translating these 4 V-class n-type motifs into soluble, structurally tunable redoxmers could open a viable pathway toward significantly higher cell voltages in NAORFBs [103].

4 | Redox Potential Regulation of Organic Anode Materials

For the anolyte, the key challenge lies in designing organic molecules with sufficiently low redox potentials while maintaining chemical stability and solubility [92]. Lowering the reduction potential typically requires introducing strong electron-donating substituents, extending π-conjugation, or incorporating heteroatoms to modulate frontier orbital energies [89, 101–104]. However, excessive destabilization of the reduced state can trigger side reactions such as radical coupling or decomposition. Therefore, potential-tuning strategies for organic anodes must balance redox potential lowering with molecular robustness, providing a foundation for constructing stable low-potential materials in NAORFBs [105]. The redox potential data of these compounds are summarized in Table 3.

4.1 | Benzothiadiazole

2,1,3-Benzothiadiazole (BzNSN)and its derivatives are a typical class of sulfur–nitrogen heterocyclic-conjugated organic molecules (Figure 9a). Owing to the fused conjugated structure between the benzene and thiadiazole (C_2N_2S) rings, these molecules exhibit excellent electron delocalization ability and reversible single-electron reduction characteristics. Consequently, they have become a research hotspot as anode materials for NAORFBs.

In 2017, Wei et al. reported that **BzNSN-1** exhibits a high solubility of 5.7 M in pure acetonitrile and remains soluble up to 2.1 M in 2.1 M LiTFSI/MeCN. In 1.0 M LiTFSI/MeCN, this molecule shows a formal potential of –1.59 V vs. Ag/Ag^+, and when paired with DBMMB, the theoretical OCV reaches 2.36 V [46]. In 2019, Yuan et al. found that when tetraethylammonium bis(trifluoromethanesulfonyl)imide (TEATFSI) is used as the supporting electrolyte, the formal potential of **BzNSN-1** in 1.0 M TEATFSI/MeCN shifts negatively to –1.90 V vs. Ag/Ag^+. Consequently, the theoretical OCV of a BzNSN–DBMMB full cell increases to 2.60 V (Figure 9b) [110]. This difference arises from the strong electrostatic interaction between Li^+ (with a small ionic radius of ~0.76 Å and high charge density) and the

TABLE 3 | Redox potentials and solubility of some typical anode electrolyte materials in NAORFBs.

Cathode	$E_{1/2}$, V	Supporting electrolyte	Solubility	Cycling stability	Limiting failure mode	Ref
BzNSN-1	−1.58 vs. Ag/Ag+	1 M LiTFSI/ACN	2.1 M	150	High-concentration-induced viscosity increase	[46]
BzNSN-2	−1.647 vs. Ag/Ag^+	0.5 M LiTFSI/ACN	>2 M	50	Radical anion decay	[57]
BzNSN-3	−1.681 vs. Ag/Ag^+	0.5 M LiTFSI/ACN	>2 M	50	Radical anion decay	[57]
BzNSN-4	−1.537 vs. Ag/Ag^+	0.5 M LiTFSI/ACN	>2 M	50	Radical anion decay	[57]
BzNSN-5	−1.356 vs. Ag/Ag^+	0.5 M LiTFSI/ACN	>2 M	50	Radical anion decay	[57]
BzNSN-6	−2.08 vs. Fc/Fc^+	0.1 M $TBABF_4$/ACN	N/A	50	Catholyte instability	[106]
BzNNN	−2.3 vs. Fc/Fc^+	0.5 M NEt_4BF_4/DMF	>0.4 M	100	Radical anion instability	[107]
BN-1	−2.85 vs. Fc/Fc^+	0.5 M NEt_4BF_4/ACN	N/A	N/A	Radical anion instability	[107]
BN-2	−2.91 vs. Fc/Fc^+	0.5 M NEt_4BF_4/ACN	N/A	N/A	Radical anion instability	[107]
BN-3	−2.19 vs. Fc/Fc^+	0.5 M NEt_4BF_4/DMF	N/A	100	Radical anion instability	[107]
BN-4	−2.53 vs. Fc/Fc^+	0.5 M NEt_4BF_4/DMF	N/A	N/A	Radical anion instability	[107]
BN-5	−2.51 vs. Fc/Fc^+	0.5 M NEt_4BF_4/DMF	N/A	N/A	Radical anion instability	[107]
BN-6	N/A	0.5 M NEt_4BF_4/DMF	N/A	N/A	Radical anion instability	[107]
BN-7	−2.30 vs. Fc/Fc^+	0.5 M NEt_4BF_4/DMF	N/A	100	Radical anion instability	[107]
BN-8	−2.30 vs. Fc/Fc^+	0.5 M NEt_4BF_4/DMF	>0.4 M	100	Radical anion instability	[107]
BN-9	−2.25 vs. Ag/Ag^+	0.5 M NEt_4BF_4/DMF	N/A	200	Molecular decomposition	[67]
BN-10	−2.14 vs. Ag/Ag^+	0.5 M NEt_4BF_4/DMFc	N/A	200	Molecular decomposition	[67]
BN-11	−2.18 vs. Ag/Ag^+	0.5 M NEt_4BF_4/DMF	N/A	200	Molecular decomposition	[67]
BN-12	−2.45 vs. Ag/Ag^+	0.5 M NEt_4BF_4/DMF	N/A	200	Molecular decomposition	[67]
TPN-1	−2.05 vs. Fc/Fc^+	0.2 M $TBAPF_6$/ACN	1.3 M	100	Radical anion instability	[108]
TPN-2	−2.12 vs. Fc/Fc^+	0.2 M $TBAPF_6$/ACN	0.5 M	100	Radical anion instability	[108]
TPN-3	−2.05 vs. Fc/Fc^+	0.2 M $TBAPF_6$/ACN	0.2 M	100	Radical anion instability	[108]

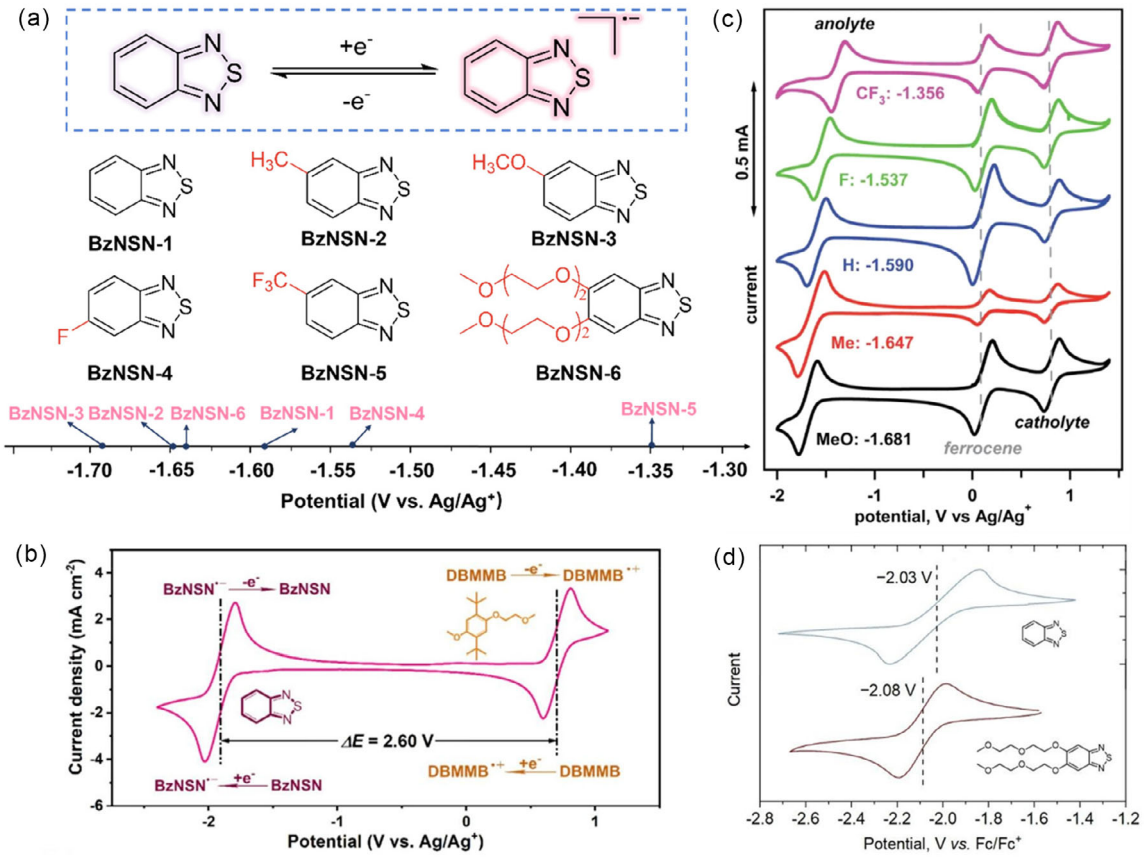

FIGURE 9 | (a) Scheme of the redox process of the BzNSN core, structures of selected BzNSN derivatives, and their potential axis distribution. (b) CV results of 10 mM BzNSN-1 and 10 mM DBMMB in 0.5 M TEATFSI/MeCN at a scan rate of 100 mV s^{-1}. Reproduced with permission [109]. Copyright 2019, Elsevier. (c) CVs of BzNSN derivatives. Reproduced with permission [57]. Copyright 2018, Royal Society of Chemistry. (d) CVs of the investigated compounds in 0.1 M $TBABF_4$/MeCN supporting electrolyte at a scan rate of 100 mV s^{-1}. Dashed lines denote $E_{1/2}$. Reproduced with permission [106]. Copyright 2022, John Wiley and Sons.

negatively charged N sites in **BzNSN-1**, forming tight ion pairs that compress the electron cloud of **BzNSN-1**, increase the reduction energy barrier, and result in a more positive formal potential. In contrast, the bulky TEA^+ cation, with its charge delocalized over four ethyl chains, has a much lower charge density and interacts weakly with **BzNSN-1**, leaving the electron cloud more delocalized. This reduces the reduction barrier and makes electron uptake easier.

In 2018, Zhang et al. investigated the effect of substituent electronic properties on the formal potential of BzNSN by introducing various single substituents (–CH_3, –OCH_3, –F, and –CF_3) at the C5 position of the benzene ring (Figure 9a) [57]. **BzNSN-2** exhibits a formal potential of −1.647 V vs. Ag/Ag^+, 57 mV more negative than unsubstituted BzNSN (–1.590 V vs. Ag/Ag^+) (Figure 9c). Since the –CH_3 is a weak EDG, the shift is minor. In contrast, the **BzNSN-3** shows a formal potential of −1.681 V vs. Ag/Ag^+, 91 mV more negative than the parent compound. The stronger p–π conjugation effect from the oxygen atom in –OCH_3 increases the electron density on the thiadiazole ring more effectively, causing a larger potential shift. Conversely, EWGs such as –F and –CF_3 decrease the electron density of the thiadiazole ring, increasing the reduction barrier and shifting the potential positively. The redox potentials of the two compounds are –1.537 V vs. Ag/Ag^+ and –1.356 V vs. Ag/Ag^+, respectively. Moreover, due to the cumulative inductive effect of multiple fluorine atoms in –CF_3, which significantly reduces the electron density of the thiadiazole ring, its redox potential is higher than that of **BzNSN-5**.

In 2022, Romadina et al. reported a new BzNSN derivative **BzNSN-6** with a distinct dual substitution pattern, introducing diethylene glycol ether chains (–$O(CH_2CH_2O)_2CH_3$) at both the C5 and C6 positions of the benzene ring. The formal potential of **BzNSN-6** is –2.08 V vs. Fc/Fc^+, about 50 mV more negative than unsubstituted BzNSN (Figure 9d). The ether-containing substituents are weak EDGs that donate electrons through the oxygen atoms' p–π conjugation, increasing the electron density of the thiadiazole ring and lowering the reduction barrier [111].

4.2 | Benzotriazole

Although 2,1,3-benzothiadiazole (**BzNSN**) features a low redox potential (–1.58 to –1.90 V vs. Ag/Ag^+) and high solubility, it still suffers from critical issues such as imbalance between negative-shifted potential and radical stability and high membrane permeability at elevated concentrations. Through a molecular design strategy of replacing sulfur atoms with nitrogen atoms and further introducing substituents, benzotriazole (**BzNNN**) and its derivatives effectively overcame the performance bottlenecks of **BzNSN**. The triazole ring in **BzNNN** possesses stronger π-electron delocalization ability than the thiadiazole ring in **BzNSN**, leading to a more negative redox potential (Figure 10a).

In 2022, Sanford et al. investigated the influence of molecular structure on the formal potential of BzNNN derivatives through site-specific N-atom substitution and functional group modification. They first compared the potential and stability differences between **BN-1** and **BN-2** substituted derivatives. **BN-1** exhibited a formal potential of −2.85 V vs. Fc/Fc^+ in 0.5 M NEt_4BF_4/MeCN, which shifted positively to −2.69 V vs. Fc/Fc^+ in DMF. **BN-2** displayed a potential of −2.91 V vs. Fc/Fc^+ in MeCN (0.06 V more negative than **BN-1**) and −2.71 V vs. Fc/Fc^+ in DMF (0.02 V more positive than **BN-1**). The negative shift arises from the distinct electronic environments of the N1 and N2 positions in the triazole ring; substitution at N2 enhances the electron-donating effect, lowers the energy of the LUMO, and thus leads to a more negative potential for **BN-2**. Furthermore, these studies suggest that DMF is a more suitable solvent than MeCN for electrochemical cycling of **BN-2** and **BN-2** [106, 109, 112]. Cyclic voltammetry studies also confirmed that methylation at the N2 position enhances redox stability compared to N1 substitution.

To further optimize redox potential and charge delocalization, Sanford et al. introduced phenyl (–Ph) and cyano (–CN) groups at different positions on the benzene ring of **BN-2**, obtaining derivatives **BN-3**, **BN-4**, and **BN-5**. In 0.5 M NEt_4BF_4/DMF, **BN-3** exhibited a formal potential of −2.19 V vs. Fc/Fc^+, 0.52 V more positive than **BN-2**. This shift results from the inductive and conjugative electron-withdrawing effects of –CN, which significantly reduce the electron density of the triazole ring and raise the reduction barrier, making electron uptake more difficult and leading to a positive potential shift. Compounds **BN-4** and **BN-5** both retained the N2-methyl substituent, with phenyl groups introduced at the C5 and C4 positions of the benzene ring, respectively. The π-electrons of the phenyl group conjugate with the BzNNN core, injecting electron density into the triazole ring via p–π conjugation, facilitating electron acceptance, and causing a negative potential shift. Consequently, **BN-4** and **BN-5** displayed formal potentials of −2.53 and −2.51 V vs. Fc/Fc^+, respectively (Figure 10c). Compound **BN-6** bearing a phenyl group at the N1 position of BzNNN exhibited irreversible redox behavior. In contrast, compound **BN-7**, with a phenyl group at the N2 position, adopts a coplanar conformation between the phenyl and triazole rings. This coplanarity enhances π-conjugation, effectively delocalizing spin density and reducing the N2-site spin density to 0.08, thus minimizing decomposition. However, **BN-7** exhibited limited solubility (0.15 M). To overcome this, the authors introduced an oligoethylene glycol (OEO) chain at the 3-position of the N2-phenyl group, yielding derivative **BN-8**. The OEO group's strong solvation ability enhanced solubility from 0.15 to ≥0.4 M in 0.5 M NEt_4BF_4/DMF, and the pure liquid form reached a concentration of 4.5 M. The redox potential

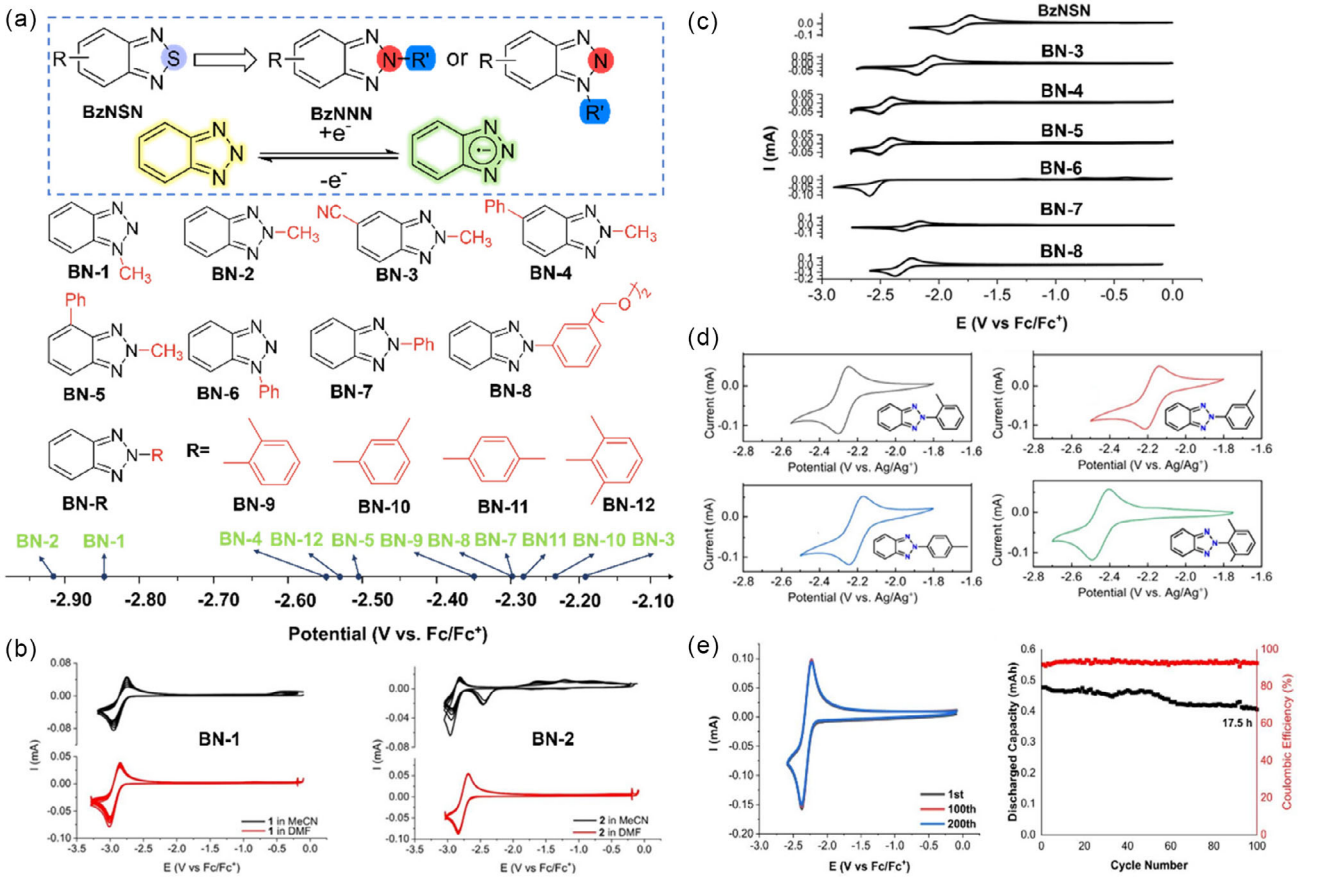

FIGURE 10 | (a) Scheme of the redox process of the BzNNN core, structures of selected BzNNN derivatives, and their potential axis distribution. (b,c) CV curves of BN-1–BN-8. Reproduced with permission [107]. Copyright 2022, American Chemical Society. (d) CVs of 5 mM solutions of BN-9–BN-12 measured in DMF with 0.5 M $TEABF_4$ at a scan rate of 100 mV s^{-1} vs. Ag/Ag^+. Reproduced with permission [67]. Copyright 2025, American Chemical Society. (e) Two hundred continuous cyclic voltammetry scans and static H-cell charge–discharge cycling experiment. Reproduced with permission [107]. Copyright 2022, American Chemical Society.

of **BN-8** remained unchanged (−2.30 V vs. Fc/Fc^+), maintaining the low-potential characteristic of **BN-7**. In electrochemical tests, **BN-8** retained 86% of its capacity after 100 charge–discharge cycles in a static H-cell. In a flow cell using 0.1 M BN-8 and 0.16 M Fc in 1 M LiTFSI/DMF, the system exhibited 86% capacity retention and >92% Coulombic efficiency after 50 cycles (17.5 h), demonstrating that OEO modification preserved **BN-7** high stability while resolving its solubility limitation, making it well-suited for NAORFBs (Figure 10e) [113].

In 2025, Gurkan et al. developed a series of BzNNN derivatives by introducing aryl groups with methyl substituents at different positions (ortho-, meta-, para-, and 2,6-dimethylphenyl) at the N2 position, yielding compound **BN-R** [67]. This systematic study revealed how sterically induced conformational changes regulate redox potential, solubility, and radical stability. **BN-9** bearing an *ortho*-methylphenyl group at N2 achieved a potential of −2.25 V vs. Ag/Ag^+, which is 670 mV more negative than that of BzNSN (−1.58 V vs. Ag/Ag^+), while maintaining a high solubility of 3.5 M in DMF. This arises from steric repulsion between the ortho-methyl group and the BzNNN ring, inducing a twisted N–N–C–C dihedral angle of 136°, disrupting π-conjugation between the BzNNN core and the aryl group, and raising the LUMO energy to −1.99 eV (compared to −2.13 eV for the coplanar conformation). The weak hyperconjugative donation of the methyl group further increases electron density on the triazole ring, slightly raising the LUMO energy. Compound **BN-10** featuring a *meta*-methylphenyl group at N2 yielded a formal potential of −2.14 V vs. Ag/Ag^+. This potential is more positive than **BN-9**, and the compound exhibited the best cycling stability (only 10% capacity loss after 200 H-cell cycles). The potential is primarily governed by the weak inductive donation of the methyl group, which slightly increases electron density and maintains a LUMO energy of −2.19 eV (higher than BzNSN but lower than **BN-9**), giving a smaller electron-acceptance barrier and a more positive potential. Compound **BN-11** bearing a *para*-methylphenyl group at N2, displayed a redox potential of −2.18 V vs. Ag/Ag^+, with stability comparable to **BN-12**. The *para*-methyl group causes no steric hindrance, preserving a coplanar geometry, while its strong p–π conjugation efficiently transfers electron density to the triazole ring, raising the LUMO energy to −2.16 eV (lower than **BN-9** −1.99 eV but higher than **BN-10** −2.19 eV), producing an intermediate potential and ensuring good radical stability. Compound **BN-12** was obtained by introducing a 2,6-dimethylphenyl group at the N2 position of BzNNN, achieving a low potential of −2.45 V vs. Ag/Ag^+. This potential represents a 200 mV negative shift compared to compound **BN-9** (−2.25 V vs. Ag/Ag^+), making it the molecule with the most negative potential in this series. This arises from strong steric repulsion between two ortho-methyl groups, enforcing a near-orthogonal N–N–C–C dihedral angle of 103°, which nearly disrupts π-conjugation. DFT calculations show the LUMO energy significantly increased to −1.81 eV (far higher than **BN-9**), thereby minimizing the electron-acceptance barrier. The high N–C bond rotation barrier (12.3 kcal mol^{-1}) locks the molecule into this twisted conformation, preventing relaxation to a coplanar state and maintaining the elevated LUMO level yielding a nonlinear, strongly negative potential shift far exceeding the additive electronic effects.

4.3 | Terephthalonitriles

Terephthalonitriles and their derivatives (Figure 11a) show great potential as anode materials for NAORFBs due to their simple

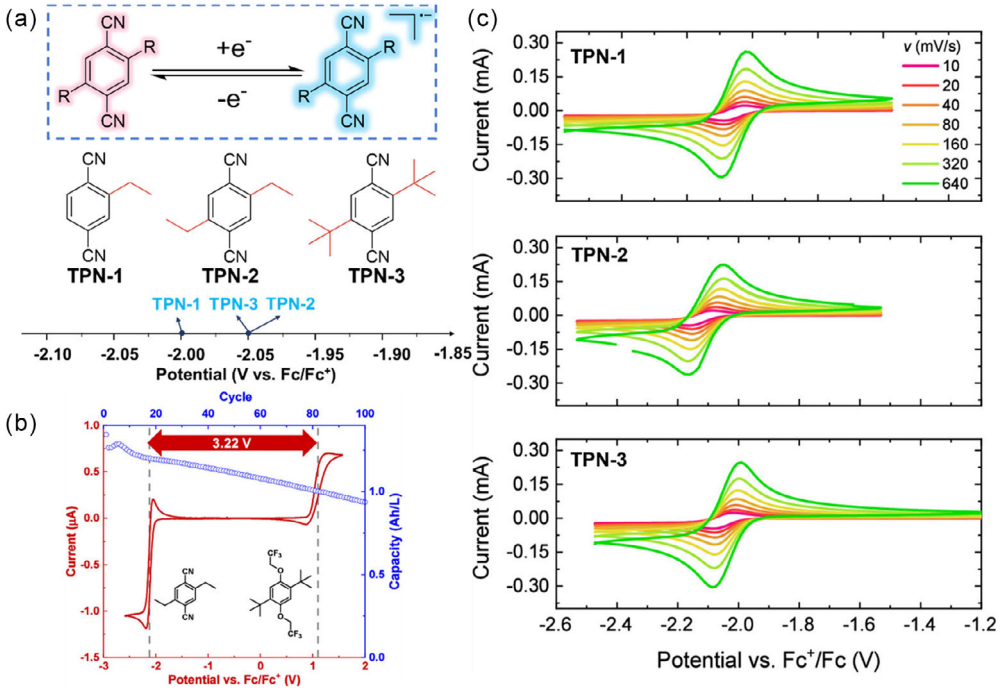

FIGURE 11 | (a) Scheme of the redox process of the terephthalonitriles core, structures of selected terephthalonitriles derivatives, and their potential axis distribution. (b) Performance of the flow battery with TPN-2 as the anode and TPN-3 as the cathode, including cyclic voltammetry (red) and 100-cycle capacity retention curve (blue), with an operating voltage of 3.22 V. Reproduced with permission [108]. Copyright 2025, American Chemical Society. (c) CV curves of 5 mM solutions of TPN-1, TPN-2, and TPN-3 (in acetonitrile containing 200 mM $TBAPF_6$) at scan rates from 10 to 640 mV s^{-1}. Reproduced with permission [108]. Copyright 2025, American Chemical Society.

and cost-effective synthesis, combined with the ability to achieve low redox potentials and form stable radical anions [107, 117–122]. By balancing redox potential regulation with enhanced cycling stability through rational substituent design, terephthalonitrile-based anodes demonstrate potential for achieving higher cell voltages and improved energy densities in NAORFBs [123].

In 2025, Jassen et al. investigated alkyl-substituted terephthalonitriles as anodes for NAORFBs, focusing on achieving high cell voltages through deep reduction potentials and improved stability. **TPN-1** is a monoethyl-substituted terephthalonitrile, while **TPN-2** is a diethyl-substituted terephthalonitrile. The redox potential of **TPN-2** is −2.12 V vs. Fc/Fc^+, which is 70 mV more negative than that of **TPN-1** (−2.05 V vs. Fc^+/Fc). This phenomenon stems from the electronic effect: As a weak EDG, ethyl enables diethyl-substituted DET to donate more electrons to the conjugated system of the benzene ring and cyano groups (–CN) compared to monoethyl-substituted **TPN-1**, resulting in a higher electron cloud density of the system. Therefore, the redox potential of **TPN-2** is more negative than that of ET. **TPN-3** is a di-tert-butyl-substituted terephthalonitrile. Although tert-butyl has greater steric hindrance, its electron-donating ability is similar to that of ethyl; thus, the redox potential of **TPN-3** is consistent with that of **TPN-1**. It is worth noting that the core role of steric hindrance lies in inhibiting the degradation of the reduced radical anions. This characteristic allows TPN-3 to maintain the same potential as **TPN-1** while achieving better cycling stability [124].

5 | Conclusions

The development of high-voltage, high-capacity NAORFBs has progressed substantially, driven by advances in organic cathodes and anodes. Regulation of redox potential is central to performance optimization, enabling higher operating voltages and improved energy densities. High-potential cathodes, including tetrathiafulvalene derivatives and cyclopropenium cations, show strong potential owing to molecular modifications that enhance electrochemical stability and redox reversibility under high-voltage conditions. Likewise, low-potential anodes, particularly terephthalonitrile-based and other electron-rich compounds, have been engineered to achieve deep reduction potentials with improved cycling stability. Despite these advances, key challenges remain. A primary issue is balancing redox potential with solubility and cycling stability. Many high-potential organic materials undergo degradation under extreme voltage conditions, leading to capacity fading and shortened cycle life. Understanding degradation mechanisms and developing materials stable at both high and low potentials are therefore critical.

6 | Perspectives

Future progress in NAORFBs requires the simultaneous optimization of redox potential, chemical stability, and solubility. Developing multifunctional organic materials with balanced electrochemical properties and long-term reversibility in nonaqueous electrolytes is a key direction. Hybrid or composite systems incorporating multiple redox-active sites may further improve energy density and cycling stability. In addition, advanced computational tools, particularly DFT, will play an important role in the rational design of redox-active molecules by predicting electronic structures and identifying optimal molecular configurations. Electrolyte optimization is another major focus. Improvements in solvents, salts, and functional additives are essential to enhance cycling stability and widen the electrochemical window, thereby ensuring stable redox processes in NAORFBs. System-level integration with large-scale renewable energy applications also requires continued effort. Owing to their scalability and suitability for long-duration storage, NAORFBs are well positioned for grid-scale energy storage. As intermittent sources such as wind and solar power expand, efficient storage of surplus electricity becomes increasingly important for grid stability. With their high energy density, long cycle life, and environmental compatibility, NAORFBs can contribute to mitigating renewable energy intermittency and supporting the transition to low-carbon power systems.

In summary, although substantial progress has been achieved, further advances in material design, electrolyte engineering, and computational methods are necessary to address remaining challenges. Continued development in these areas will strengthen the role of NAORFBs in large-scale, sustainable energy storage.

Author Contributions

Jia Zhu, Yichao Yan, and Zhong Jin supervised and coordinated the project. Li Wang, Yuanlin Zou, Qinwen Zhu, Yu Qin, and Jiayi Huang were responsible for collecting the data and preparing and revising the manuscript. Li Wang and Yuanlin Zou wrote the manuscript and contributed equally to this work.

Acknowledgments

This work was supported by the National Natural Science Foundation of China (U25A20628, 22561160129, 22479074, 22475096, and 22509084), the Equipment Pre-Research and Ministry of Education Joint Fund (8091B02052407), the Fundamental Research Program Key Project of Jiangsu Province (BK20253008), the Natural Science Foundation of Jiangsu Province (BK20240400, BK20241236, and BK20251236), the Science and Technology Major Project of Jiangsu Province (BG2024013), the Scientific and Technological Achievements Transformation Special Fund of Jiangsu Province (BA2023037), the Academic Degree and Postgraduate Education Reforming Project of Jiangsu Province (JGKT24_C001), the Key Core Technology Open Competition Project of Suzhou City (SYG2024122, SYG2024123), the Open Research Fund of Suzhou Laboratory (SZLAB-1308-2024-TS005), the Jiangsu Provincial Graduate Research and Practice Innovation Program (SJCX25_0044), and the Chenzhou National Sustainable Development Agenda Innovation Demonstration Zone Provincial Special Project (2023sfq11).

Funding

This study was funded by the National Natural Science Foundation of China (U25A20628, 22561160129, 22479074, 22475096, and 22509084), the Equipment Pre-Research and Ministry of Education Joint Fund (8091B02052407), the Fundamental Research Program Key Project of Jiangsu Province (BK20253008), the Natural Science Foundation of Jiangsu Province (BK20240400, BK20241236, and BK20251236), the Science and Technology Major Project of Jiangsu Province (BG2024013), the Scientific and Technological Achievements Transformation Special Fund of Jiangsu Province (BA2023037), the Academic Degree and Postgraduate Education Reforming Project of Jiangsu Province (JGKT24_C001), the Key Core Technology Open Competition Project of Suzhou City (SYG2024122, SYG2024123), the Open Research Fund of Suzhou Laboratory (SZLAB-1308-2024-TS005), the Jiangsu Provincial Graduate Research and Practice Innovation

Program (SJCX25_0044), and the Chenzhou National Sustainable Development Agenda Innovation Demonstration Zone Provincial Special Project (2023sfq11).

Conflicts of Interest

The authors declare no conflicts of interest.

References

1. C. M. Davis, C. E. Boronski, T. Yang, T. Liu, and Z. Liang, "Molecular Engineering of Redox Couples for Non-Aqueous Redox Flow Batteries," *Batteries* 9, no. 10 (2023): 504.

2. Y. Ding, C. Zhang, L. Zhang, Y. Zhou, and G. Yu, "Molecular Engineering of Organic Electroactive Materials for Redox Flow Batteries," *Chemical Society Reviews* 47 (2018): 69–103.

3. M. L. Lehmann, L. Tyler, E. C. Self, G. Yang, J. Nanda, and T. Saito, "Membrane Design for Non-Aqueous Redox Flow Batteries: Current Status and Path Forward," *Chem* 8 (2022): 1611–1636.

4. T. Dai, B. Yang, J. Wei, et al., "Environmentally Benign and Long Cycling Mn-Ion Full Batteries Enabled by Hydrated Eutectic Electrolytes and Polycarbonyl Conjugated Organic Anodes," *Journal of the American Chemical Society* 147, no. 16 (2025): 13721–13731.

5. J. A. Dowling, K. Z. Rinaldi, T. H. Ruggles, et al., "Role of Long-Duration Energy Storage in Variable Renewable Electricity Systems," *Joule* 4 (2020): 1907–1928.

6. D. G. Kwabi, Y. Ji, and M. J. Aziz, "Electrolyte Lifetime in Aqueous Organic Redox Flow Batteries: A Critical Review," *Chemical Reviews* 120 (2020): 6467–6489.

7. A. Cherp, V. Vinichenko, J. Tosun, J. A. Gordon, and J. Jewell, "National Growth Dynamics of Wind and Solar Power Compared to the Growth Required for Global Climate Targets," *Nature Energy* 6 (2021): 742–754.

8. Z. Zhu, T. Jiang, M. Ali, et al., "Rechargeable Batteries for Grid Scale Energy Storage," *Chemical Reviews* 122 (2022): 16610–16751.

9. L. Su, M. Ferrandon, J. A. Kowalski, J. T. Vaughey, and F. R. Brushett, "Electrolyte Development for Non-Aqueous Redox Flow Batteries Using a High-Throughput Screening Platform," *Journal of the Electrochemical Society* 161 (2014): A1905–A1914.

10. M. Li, J. Case, and S. D. Minteer, "Bipolar Redox-Active Molecules in Non-Aqueous Organic Redox Flow Batteries: Status and Challenges," *ChemElectroChem* 8 (2021): 1215–1232.

11. Z. Li, T. Jiang, M. Ali, C. Wu, and W. Chen, "Recent Progress in Organic Species for Redox Flow Batteries," *Energy Storage Materials* 50 (2022): 105–138.

12. L. Liu, G. He, M. Wu, et al., "Climate Change Impacts on Planned Supply–demand Match in Global Wind and Solar Energy Systems," *Nature Energy* 8 (2023): 870–880.

13. M. Armand and J.-M. Tarascon, "Building Better Batteries," *Nature* 451 (2008): 451.

14. J. Xiao, F. Shi, T. Glossmann, C. Burnett, and Z. Liu, "From Laboratory Innovations to Materials Manufacturing for Lithium-Based Batteries," *Nature Energy* 8 (2023): 329–339.

15. K. R. Ngoy, V. T. Lukong, K. O. Yoro, et al., "Lithium-Ion Batteries and the Future of Sustainable Energy: A Comprehensive Review," *Renewable and Sustainable Energy Reviews* 223 (2025): 115971.

16. G.-T. Park, N.-Y. Park, J.-H. Ryu, et al., "Zero-Strain Mn-Rich Layered Cathode for Sustainable and High-Energy Next-Generation Batteries," *Nature* 10 (2025): 1215–1225.

17. N. H. Attanayake, Z. Liang, Y. Wang, et al., "Dual Function Organic Active Materials for Nonaqueous Redox Flow Batteries," *Materials Advances* 2 (2021): 1390–1401.

18. J. Back, G. Kwon, J. E. Byeon, H. Song, K. Kang, and E. Lee, "Tunable Redox-Active Triazenyl–Carbene Platforms: A New Class of Anolytes for Non-Aqueous Organic Redox Flow Batteries," *ACS Applied Materials & Interfaces* 12 (2020): 37338–37345.

19. C. Balischewski, B. Bhattacharyya, J. J. Bailey, et al., "Elucidating the Iron-Based Ionic Liquid $[C_4py][FeCl_4]$: Structural Insights and Potential for Nonaqueous Redox Flow Batteries," *Advanced Functional Materials* 34 (2024): 2311571.

20. Y. Ding, Y. Li, and G. Yu, "Exploring Bio-Inspired Quinone-Based Organic Redox Flow Batteries: A Combined Experimental and Computational Study," *Chem* 1 (2016): 790–801.

21. M. Mansha, A. Anam, S. Akram Khan, et al., "Recent Developments on Electroactive Organic Electrolytes for Non-Aqueous Redox Flow Batteries: Current Status, Challenges, and Prospects," *Chemical Record* 24 (2024): e202300233.

22. Z. Rhodes, J. R. Cabrera-Pardo, M. Li, and S. D. Minteer, "Electrochemical Advances in Non-Aqueous Redox Flow Batteries," *Israel Journal of Chemistry* 61 (2020): 101–112.

23. L. A. Robertson, M. Afsar Uddin, I. A. Shkrob, J. S. Moore, and L. Zhang, "Liquid Redoxmers for Nonaqueous Redox Flow Batteries," *ChemSusChem* 16 (2023): e202300043.

24. T. Janoschka, N. Martin, U. Martin, et al., "An Aqueous, Polymer-Based Redox-Flow Battery Using Non-Corrosive, Safe, and Low-Cost Materials," *Nature* 527 (2015): 78–81.

25. J. D. Hunt, E. Byers, Y. Wada, et al., "Global Resource Potential of Seasonal Pumped Hydropower Storage for Energy and Water Storage," *Nature Communications* 11 (2020): 947.

26. P. C. Nikolaos, F. Marios, and K. Dimitris, "A Review of Pumped Hydro Storage Systems," *Energies* 16 (2023): 4516.

27. F. Odoi-Yorke, A. A. Abbey, T. A. Frimpong, et al., "A Bird's Eye View of Pumped Hydro Energy Storage: A Bibliometric Analysis of Global Research Trends and Future Directions," *Journal of Energy Storage* 103 (2024): 114339.

28. B. G. Tegegne, A. W. Bayeh, D. M. Kabtamu, A. M. Demeku, and C.-H. Wang, *Chemical Engineering Journal* 501 (2024): 157792.

29. X. Wei, W. Pan, W. Duan, et al., "Materials and Systems for Organic Redox Flow Batteries: Status and Challenges," *ACS Energy Letters* 2 (2017): 2187–2204.

30. D. Xu, C. Zhang, and Y. Li, "Molecular Engineering Redox-Active Organic Materials for Nonaqueous Redox Flow Battery," *Current Opinion in Chemical Engineering* 37 (2022): 100851.

31. C. Ponce de León, A. Frías-Ferrer, J. González-García, D. A. Szánto, and F. C. Walsh, "Redox Flow Cells for Energy Conversion," *Journal of Power Sources* 160 (2006): 716–732.

32. C. Zhang, Z. Yuan, and X. Li, "Designing Better Flow Batteries: An Overview on Fifty Years' Research," *ACS Energy Letters* 9 (2024): 3456–3473.

33. W. Wang and V. Sprenkle, "Redox Flow Batteries Go Organic," *Nature Chemistry* 8 (2016): 204–206.

34. X. Fang, Z. Li, L. Zeng, et al., "Kinetic Control over Disproportionation Stabilizes Wurster's Blue Catholyte for Nonaqueous Redox Flow Batteries," *ACS Energy Letters* 9 (2024): 5737–5743.

35. R. R. Jacquemond, R. Geveling, A. Forner-Cuenca, and K. Nijmeijer, "On the Characterization of Membrane Transport Phenomena and Ion Exchange Capacity for Non-Aqueous Redox Flow Batteries," *Journal of the Electrochemical Society* 169 (2022): 080528.

36. J. Yuan, Z.-Z. Pan, Y. Jin, et al., "Membranes in Non-Aqueous Redox Flow Battery: A Review," *Journal of Power Sources* 500 (2021): 229983.

37. D. Yue, W. Zhang, I. Zhao, et al., "A New Nonaqueous Flow Battery with Extended Cycling," *Reactions* 5 (2024): 452–461.

38. S. Samaroo, C. Hengesbach, C. Bruggeman, et al., "C–H···π Interactions Disrupt Electrostatic Interactions between Non-Aqueous Electrolytes to Increase Solubility," *Nature Chemistry* 15 (2023): 1365–1373.

39. Y. Matsuda, K. Tanaka, M. Okada, Y. Takasu, and M. Morita, "A Rechargeable Redox Battery Utilizing Ruthenium Complexes with Non-Aqueous Organic Electrolyte," *Journal of Applied Electrochemistry* 18 (1988): 909–914.

40. T. Yamamura, Y. Shiokawa, H. Yamana, and H. Moriyama, "Electrochemical Investigation of Uranium β-Diketonates for All-Uranium Redox Flow Battery," *Electrochimica Acta* 48 (2002): 43–50.

41. M. H. Chakrabarti, R. A. W. Dryfe, and E. P. L. Roberts, "Evaluation of Electrolytes for Redox Flow Battery Applications," *Electrochimica Acta* 52 (2007): 2189–2195.

42. Q. Liu, A. E. S. Sleightholme, A. A. Shinkle, Y. Li, and L. T. Thompson, "Non-Aqueous Vanadium Acetylacetonate Electrolyte for Redox Flow Batteries," *Electrochemistry Communications* 11 (2009): 2312–2315.

43. Q. Liu, A. A. Shinkle, Y. Li, C. W. Monroe, L. T. Thompson, and A. E. S. Sleightholme, "Non-Aqueous Chromium Acetylacetonate Electrolyte for Redox Flow Batteries," *Electrochemistry Communications* 12 (2010): 1634–1637.

44. J.-H. Kim, K. J. Kim, M.-S. Park, et al., "Development of Metal-Based Electrodes for Non-Aqueous Redox Flow Batteries," *Electrochemistry Communications* 13 (2011): 997–1000.

45. Y. Ding, Y. Zhao, Y. Li, J. B. Goodenough, and G. Yu, "A High-Performance All-Metallocene-Based, Non-Aqueous Redox Flow Battery," *Energy & Environmental Science* 10 (2017): 491–497.

46. W. Duan, J. Huang, J. A. Kowalski, et al., ""Wine-Dark Sea" in an Organic Flow Battery: Storing Negative Charge in 2,1,3-Benzothiadiazole Radicals Leads to Improved Cyclability," *ACS Energy Letters* 2 (2017): 1156–1161.

47. B. Hu, C. DeBruler, Z. Rhodes, and T. L. Liu, "Long-Cycling Aqueous Organic Redox Flow Battery (AORFB) toward Sustainable and Safe Energy Storage," *Journal of the American Chemical Society* 139 (2017): 1207–1214.

48. L. Zhang, R. Feng, W. Wang, and G. Yu, "Emerging Chemistries and Molecular Designs for Flow Batteries," *Nature Reviews Chemistry* 6 (2022): 524–543.

49. H. Zhou, R. Zhang, Q. Ma, et al., "Modeling and Simulation of Non-Aqueous Redox Flow Batteries: A Mini-Review," *Batteries* 9 (2023): 215.

50. S. Peng, L. Zhang, C. Zhang, et al., "Gradient-Distributed Metal–Organic Framework–Based Porous Membranes for Nonaqueous Redox Flow Batteries," *Advanced Energy Materials* 8 (2018): 1802533.

51. G. Kwon, K. Lee, M. H. Lee, et al., "Bio-Inspired Molecular Redesign of a Multi-Redox Catholyte for High-Energy Non-Aqueous Organic Redox Flow Batteries," *Chem* 5 (2019): 2642–2656.

52. R. Tort, O. Westhead, M. Spry, et al., "Nonaqueous Li-Mediated Nitrogen Reduction: Taking Control of Potentials," *ACS Energy Letters* 8 (2023): 1003–1009.

53. W. Alnoush, R. Black, and D. Higgins, "Judicious Selection, Validation, and use of Reference Electrodes for In Situ and Operando Electrocatalysis Studies," *Chem Catalysis* 1 (2021): 997–1013.

54. E. C. Cengiz, J. Rizell, M. Sadd, A. Matic, and N. Mozhzhukhina, "Review—Reference Electrodes in Li-Ion and Next Generation Batteries: Correct Potential Assessment, Applications and Practices," *Journal of the Electrochemical Society* 168 (2021): 120539.

55. C. Zhang, Y. Qian, Y. Ding, et al., "Biredox Eutectic Electrolytes Derived From Organic Redox-Active Molecules: High-Energy Storage Systems," *Angewandte Chemie International Edition* 58 (2019): 7045–7050.

56. M. Li, Z. Rhodes, J. R. Cabrera-Pardo, and S. D. Minteer, "Recent Advancements in Rational Design of Non-Aqueous Organic Redox Flow Batteries," *Sustainable Energy & Fuels* 4 (2020): 4370–4389.

57. J. Huang, W. Duan, J. Zhang, et al., "Substituted Thiadiazoles as Energy-Rich Anolytes for Nonaqueous Redox Flow Cells," *Journal of Materials Chemistry A* 6 (2018): 6251–6254.

58. M. Schmucker, T. A. Gully, A. Schmidt, et al., "Investigations toward a Non-Aqueous Hybrid Redox-Flow Battery with a Manganese-Based Anolyte and Catholyte," *Advanced Energy Materials* 11 (2021): 2101261.

59. K. H. Jung, G. S. Jeong, C. Y. Go, and K. C. Kim, "Conjugacy of Organic Cathode Materials for High-Potential Lithium-Ion Batteries: Carbonitriles versus Quinones," *Energy Storage Materials* 24 (2020): 237–246.

60. Y. Qin, V. Sethuraman, S. G. Choi, et al., "Conjugation Effect of Amine Molecules in Non-Aqueous Mg Redox Flow Batteries," *Chemical Science* 16 (2025): 16205–16217.

61. S. Sharma, G. A. Andrade, S. Maurya, et al., "Iron-Iminopyridine Complexes as Charge Carriers for Non-Aqueous Redox Flow Battery Applications," *Energy Storage Materials* 37 (2021): 576–586.

62. A. Banik, U. Sengupta, H. Hughes, et al., "Molecular Design Considerations for Azobenzene Anolytes," *ACS Omega* 10 (2025): 26199–26206.

63. T. Liu, J. Yuan, Y. Zhen, C. Zhang, and Y. Li, "Porous Poly(vinylidene Fluoride) (PVDF) Membrane with 2D Vermiculite Nanosheets Modification for Non-Aqueous Redox Flow Batteries," *Journal of Membrane Science* 651 (2022): 120468.

64. P. Lu, P. Sun, Q. Ma, et al., "Rationally Designed Ternary Deep Eutectic Solvent Enabling Higher Performance for Non-Aqueous Redox Flow Batteries," *Processes* 10 (2022): 649.

65. B. Tang, J. Zhao, J. F. Xu, and X. Zhang, "Tuning the Stability of Organic Radicals: From Covalent Approaches to Non-Covalent Approaches," *Chemical Science* 11 (2020): 1192–1204.

66. Y. Yan, D. B. Vogt, T. P. Vaid, M. S. Sigman, and M. S. Sanford, "Development of High Energy Density Diaminocyclopropenium-Phenothiazine Hybrid Catholytes for Non-Aqueous Redox Flow Batteries," *Angewandte Chemie International Edition* 60 (2021): 27039–27045.

67. P. Sabhapathy, U. Sengupta, M. Munoz, et al., "Conformational Control as a Design Strategy to Tune the Redox Behavior of Benzotriazole Negolytes for Nonaqueous Flow Batteries," *ACS Applied Materials & Interfaces* 17 (2025): 19607–19616.

68. Y. Zhao, Z. Yu, L. A. Robertson, et al., "Unexpected Electrochemical Behavior of an Anolyte Redoxmer in Flow Battery Electrolytes: Solvating Cations Help to Fight against the Thermodynamic–kinetic Dilemma," *Journal of Materials Chemistry A* 8 (2020): 13470–13479.

69. Q. Ma, W. Fu, J. Xu, Z. Wang, and Q. Xu, "Study on the Optimal Double-Layer Electrode for a Non-Aqueous Vanadium-Iron Redox Flow Battery Using a Machine Learning Model Coupled with Genetic Algorithm," *Processes* 11 (2023): 1529.

70. M. Li, S. A. Odom, A. R. Pancoast, et al., "Experimental Protocols for Studying Organic Non-Aqueous Redox Flow Batteries," *ACS Energy Letters* 6 (2021): 3932–3943.

71. V. Pavlishchuk and A. Addison, "Conversion Constants for Redox Potentials Measured versus Different Reference Electrodes in Acetonitrile Solutions at 25°C," *Inorganica Chimica Acta* 298 (2000): 97–102.

72. M. Golovin, D. Wilkinson, J. Dudley, D. Holonko, and S. Woo, "Applications of Metallocenes in Rechargeable Lithium Batteries for Overcharge Protection," *Journal of the Electrochemical Society* 139 (1992): 5–10.

73. Y. Yan, T. P.Vaid, and M. S.Sanford, "Bis(diisopropylamino)cyclopropenium-Arene Cations as High Oxidation Potential and High Stability Catholytes for Non-Aqueous Redox Flow Batteries," *Journal of the American Chemical Society* 142 (2020): 17564–17571.

74. S. G. Robinson, Y. Yan, K. H. Hendriks, M. S. Sanford, and M. S. Sigman, "Developing a Predictive Solubility Model for

Monomeric and Oligomeric Cyclopropenium-Based Flow Battery Catholytes," *Journal of the American Chemical Society* 141 (2019): 10171–10176.

75. X. Wei, L. Cosimbescu, W. Xu, et al., "Towards High-Performance Nonaqueous Redox Flow Electrolyte Via Ionic Modification of Active Species," *Advanced Energy Materials* 5 (2014): 1400678.

76. L. Cosimbescu, X. Wei, M. Vijayakumar, et al., "Anion-Tunable Properties and Electrochemical Performance of Functionalized Ferrocene Compounds," *Scientific Reports* 5 (2015): 14117.

77. B. Hwang, M. S. Park, and K. Kim, "Ferrocene and Cobaltocene Derivatives for Non-Aqueous Redox Flow Batteries," *ChemSusChem* 8 (2015): 310–314.

78. G. Cong, Y. Zhou, Z. Li, and Y.-C. Lu, "A Highly Concentrated Catholyte Enabled by a Low-Melting-Point Ferrocene Derivative," *ACS Energy Letters* 2 (2017): 869–875.

79. Q. Huang, H. Li, M. Gratzel, and Q. Wang, "Reversible Chemical Delithiation/Lithiation of $LiFePO_4$: Towards a Redox Flow Lithium-Ion Battery," *Physical Chemistry Chemical Physics* 15 (2013): 1793–1797.

80. H. S. Kim, T. Yoon, Y. Kim, S. Hwang, J. H. Ryu, and S. M. Oh, "Increase of Both Solubility and Working Voltage by Acetyl Substitution on Ferrocene for Non-Aqueous Flow Battery," *Electrochemistry Communications* 69 (2016): 72–75.

81. J. A. Kowalski, M. D. Casselman, A. P. Kaur, et al., "A Stable Two-Electron-Donating Phenothiazine for Application in Nonaqueous Redox Flow Batteries," *Journal of Materials Chemistry A* 5 (2017): 24371–24379.

82. N. H. Attanayake, J. A. Kowalski, K. V. Greco, et al., "Tailoring Two-Electron-Donating Phenothiazines To Enable High-Concentration Redox Electrolytes for Use in Nonaqueous Redox Flow Batteries," *Chemistry of Materials* 31 (2019): 4353–4363.

83. X. Wei, W. Xu, M. Vijayakumar, et al., "TEMPO-Based Catholyte for High-Energy Density Nonaqueous Redox Flow Batteries," *Advanced Materials* 26 (2014): 7649–7653.

84. B. Ok, W. Na, T.-H. Kwon, et al., "Understanding the Enhanced Electrochemical Performance of TEMPO Derivatives in Non-Aqueous Lithium Ion Redox Flow Batteries," *Journal of Industrial and Engineering Chemistry* 80 (2019): 545–550.

85. J. D. Milshtein, J. L. Barton, R. M. Darling, and F. R. Brushett, "4-Acetamido-2,2,6,6-Tetramethylpiperidine-1-Oxyl as a Model Organic Redox Active Compound for Nonaqueous Flow Batteries," *Journal of Power Sources* 327 (2016): 151–159.

86. Y. Zhao, J. Zhang, G. Agarwal, et al., "TEMPO Allegro: Liquid Catholyte Redoxmers for Nonaqueous Redox Flow Batteries," *Journal of Materials Chemistry A* 9 (2021): 16769–16775.

87. N. Daub, K. H. Hendriks, and R. A. J. Janssen, "Two-Electron Tetrathiafulvalene Catholytes for Nonaqueous Redox Flow Batteries," *Batteries & Supercaps* 5 (2022): e202200386.

88. W. Hu, J. Xu, N. Chen, Z. Deng, Y. Lai, and D. Chen, "Tetrathiafulvalene esters with high redox potentials and improved solubilities for non-aqueous redox flow battery applications," *Green Energy & Environment* 9 (2024): 899–908.

89. X. Wang, A. Lashgari, R. Siwakoti, et al., "Tetrathiafulvalene (TTF) Derivatives as Catholytes for Dual-Type Redox Flow Batteries: Molecular Engineering Enables High Energy Density and Cyclability," *Journal of Materials Chemistry A* 11 (2023): 19056–19065.

90. J. McGrath, R. K. Gautam, X. Wang, and J. J. Jiang, "High-Voltage Catholyte for High-Energy-Density Nonaqueous Redox Flow Battery," *Angewandte Chemie International Edition* 63 (2024): e202407906.

91. C. S. Sevov, S. K. Samaroo, and M. S. Sanford, "Cyclopropenium Salts as Cyclable, High-Potential Catholytes in Nonaqueous Media," *Advanced Energy Materials* 7 (2016): 1602027.

92. Y. Yan, S. G. Robinson, M. S. Sigman, and M. S. Sanford, "Mechanism-Based Design of a High-Potential Catholyte Enables a 3.2 V All-Organic Nonaqueous Redox Flow Battery," *Journal of the American Chemical Society* 141 (2019): 15301–15306.

93. Y. Ding, Y. Zhao, and G. Yu, "A Membrane-Free Ferrocene-Based High-Rate Semiliquid Battery," *Nano Letters* 15 (2015): 4108–4113.

94. Y. Zhao, Y. Ding, J. Song, et al., "Sustainable Electrical Energy Storage through the Ferrocene/Ferrocenium Redox Reaction in Aprotic Electrolyte," *Angewandte Chemie International Edition* 53 (2014): 11036–11040.

95. W. Ren, E. Zhou, B. Fang, et al., "Experimental and Computational Studies on the Reactivity of a Terminal Thorium Imidometallocene Towards Organic Azides and Diazoalkanes," *Angewandte Chemie International Edition* 53 (2014): 11310–11314.

96. K. Park, J. H. Cho, K. Shanmuganathan, et al., "New Battery Strategies with a Polymer/Al_2O_3 Separator," *Journal of Power Sources* 263 (2014): 52–58.

97. J. D. Milshtein, A. P. Kaur, M. D. Casselman, et al., "High Current Density, Long Duration Cycling of Soluble Organic Active Species for Non-Aqueous Redox Flow Batteries," *Energy & Environmental Science* 9 (2016): 3531–3543.

98. J. A. Kowalski, L. Su, J. D. Milshtein, and F. R. Brushett, "Recent Advances in Molecular Engineering of Redox Active Organic Molecules for Nonaqueous Flow Batteries," *Current Opinion in Chemical Engineering* 13 (2016): 45–52.

99. Y. Yan, R. Walser-Kuntz, and M. S. Sanford, "Targeted Optimization of Phenoxazine Redox Center for Nonaqueous Redox Flow Batteries," *ACS Materials Letters* 4 (2022): 733–739.

100. L. H. Sommer, J. McLick, and C. M. Golino, "Electrical Conductivity by the bis(1,3-dithiole)-bis(1,3-dithiolium) System," *Journal of the American Chemical Society* 94 (1972): 670–671.

101. J. Wang, P. Apostol, D. Rambabu, et al., "Revealing the Reversible Solid-State Electrochemistry of Lithium-Containing Conjugated Oximates for Organic Batteries," *Science Advances* 9 (2023): 6079.

102. X. Zhou, C. Xu, X. Guo, et al., "Computational and Machine Learning-Assisted Discovery and Experimental Validation of Conjugated Sulfonamide Cathodes for Lithium-Ion Batteries," *Advanced Energy Materials* 15 (2025): 2401658.

103. X. Guo, P. Apostol, X. Zhou, et al., "Towards the 4 V-Class n-Type Organic Lithium-Ion Positive Electrode Materials: the Case of Conjugated Triflimides and Cyanamides," *Energy & Environmental Science* 17 (2024): 173–182.

104. C. S. Sevov, R. E. Brooner, E. Chenard, et al., "Evolutionary Design of Low Molecular Weight Organic Anolyte Materials for Applications in Nonaqueous Redox Flow Batteries," *Journal of the American Chemical Society* 137 (2015): 14465–14472.

105. N. Chen, D. Chen, J. Wu, Y. Lai, and D. Chen, *Chemical Engineering Journal* 462 (2023): 141996.

106. M. V. Makarova, A. V. Akkuratov, M. E. Sideltsev, K. J. Stevenson, and E. I. Romadina, "Novel Ethylene Glycol Substituted Benzoxadiazole and Benzothiadiazole as Anolytes for Nonaqueous Organic Redox Flow Batteries," *ChemElectroChem* 9 (2022): e202200483.

107. Y. Yan, L. Zhang, R. Walser-Kuntz, et al., "Benzotriazoles as Low-Potential Anolytes for Non-Aqueous Redox Flow Batteries," *Chemistry of Materials* 34 (2022): 10594–10605.

108. N. Daub, X. Zhang, N. J. L. van Rijswijk, P. de Silva, and R. A. J. Janssen, "Supra-3-V Nonaqueous Redox-Flow Batteries Based on Simple Terephthalonitrile Anolytes," *ACS Applied Energy Materials* 8 (2025): 15124–15133.

109. J. Yuan, C. Zhang, Y. Zhen, Y. Zhao, and Y. Li, "Enhancing the Performance of an All-Organic Non-Aqueous Redox Flow Battery," *Journal of Power Sources* 443 (2019): 227283.

110. Y. Cho, H. Kye, B.-G. Kim, and J. E. Kwon, "Redox Active Viologen Derivatives for Aqueous and Non-Aqueous Organic Redox Flow Batteries Applications," *Journal of Industrial and Engineering Chemistry* 136 (2024): 73–88.

111. R. K. Gautam, X. Wang, and J. J. Jiang, "Membrane-Free Redox Flow Battery with Polymer Electrolytes," *Nature Communications* 16 (2025): 8830.

112. X. Wei, W. Duan, J. Huang, et al., "A High-Current, Stable Nonaqueous Organic Redox Flow Battery," *ACS Energy Letters* 1 (2016): 705–711.

113. T. Ma, Z. Pan, L. Miao, et al., "Porphyrin-Based Symmetric Redox-Flow Batteries Towards Cold-Climate Energy Storage," *Angewandte Chemie International Edition* 57 (2018): 3158–3162.

114. M. D'Adamo, N. Daub, L. Trilla, J. A. Saez-Zamora, and J. M. Paz-Garcia, "Modeling of a Non-Aqueous Redox Flow Battery for Performance and Capacity Fade Analysis," *Batteries* 11 (2024): 8.

115. Y. Mo, Z. Lu, G. Rughoobur, et al., "Microfluidic Electrochemistry for Single-Electron Transfer Redox-Neutral Reactions," *Science* 368 (2020): 1352–1357.

116. Q. Deng, S.-J. He, J. Pei, et al., "Exploitation of Redox-Active 1,4-Dicyanobenzene and 9,10-Dicyanoanthracene as the Organic Electrode Materials in Rechargeable Lithium Battery," *Electrochemistry Communications* 75 (2017): 29–32.

117. L. Zhang, Y. Qian, R. Feng, et al., "Reversible Redox Chemistry in Azobenzene-Based Organic Molecules for High-Capacity and Long-Life Nonaqueous Redox Flow Batteries," *Nature Communications* 11 (2020): 3843.

118. J. S. Jaworski and M. Cembor, "Kinetics of Protonation of Anthracene Radical Anions in DMSO by a Series of Substituted Phenols," *Journal of Physical Organic Chemistry* 16 (2003): 655–660.

119. A. Shrestha, K. H. Hendriks, M. S. Sigman, S. D. Minteer, and M. S. Sanford, "Realization of an Asymmetric Non-Aqueous Redox Flow Battery through Molecular Design to Minimize Active Species Crossover and Decomposition," *Chemistry* 26 (2020): 5369–5373.

120. Q. Qu, X. Gao, J. Gao, and G. Yuan, "A Highly Efficient Electrochemical Route for the Conversion of Aldehydes to Nitriles," *Science China Chemistry* 58 (2015): 747–750.

121. Y. Huo, X. Xing, C. Zhang, X. Wang, and Y. Li, "An All Organic Redox Flow Battery with High Cell Voltage," *RSC Advances* 9 (2019): 13128–13132.

122. X. Xing, Q. Liu, W. Xu, et al., "All-Liquid Electroactive Materials for High Energy Density Organic Flow Battery," *ACS Applied Energy Materials* 2 (2019): 2364–2369.

123. X. Xing, Q. Liu, B. Wang, J. P. Lemmon, and W. Q. Xu, "A Low Potential Solvent-Miscible 3-Methylbenzophenone Anolyte Material for High Voltage and Energy Density All-Organic Flow Battery," *Journal of Power Sources* 445 (2020): 227330.

124. X. Wang, X. Xing, Y. Huo, Y. Zhao, Y. Li, and H. Chen, "Study of Tetraethylammonium Bis(trifluoromethylsulfonyl)imide as a Supporting Electrolyte for an All-Organic Redox Flow Battery Using Benzophenone and 1,4-Di-Tert-Butyl-2,5-Dimethoxybenzene as Active Species," *International Journal of Electrochemical Science* 13 (2018): 6676–6683.